

4

Simulations with fixed analytic potentials II: barred-spiral simulations and synthetic observations

“Equipped with his five senses, man explores the universe around him and calls the adventure Science.”

–Edwin Hubble (May 1929), Harper’s Magazine 158: 732.

4.1 Introduction

In the previous chapter ISM gas was subjected to various arm and bar structures by the use of smooth analytic potentials. Alone, neither of these features provided a good match to all the observed l - v features of our Galaxy, though individual features could be reproduced. The current consensus is that the Milky Way has both bar and spiral components (Churchwell et al. 2009), and so it is not surprising that the all features cannot be reproduced with just arm or bar potentials. This leads to the next stage of our investigation; to perform calculations with both bar and spiral perturbations. In Section 4.6 we present the results of our investigation into the barred-spiral nature of the Milky Way, and our models that provide the best representation of Galactic structure.

The method to create l - v features in the previous section is simplistic in nature, and in no way takes into account the optical depth of the ISM, but instead simply approximates emission strength as decreasing with distance squared from the source gas particles. Now that a refined parameter space has been produced it is prudent to use a more sophisticated approach to creating l - v maps. A radiative transfer code is employed to create synthetic l - v maps of some of our best

Galactic models, so that emission can be directly compared with observations. In the first half of this chapter we briefly discuss the theory of radiative transfer relevant to our calculations. Tests of the method are shown before applying it to our SPH calculations from the previous chapter, and finally applying to the best-fitting barred-spiral calculations. The investigation using analytic potentials is then discussed in full in Section 4.7.

4.2 Theory of radiative transfer

The theory of radiative transfer is a way of describing the quantifiable amount of radiation received from some source, including effects of absorption and re-emission by any media in between the point of emission and observation. This is employed later in this Chapter to produce Galactic emission maps from the SPH calculations in the previous chapter, so we devote some time here to the discussion of the relevant fundamentals.

The simplest form of radiative transfer comes in the form of Beer's law, where an incident ray of intensity I_0 passes through some absorbing medium of thickness s resulting in an emergent intensity of $I = I_0 e^{-n\sigma s}$, where n is the number density and σ the cross section of absorption [cm^2]. The cross section is related to two other quantities, the absorption coefficient (α) and opacity (κ , or mass absorption coefficient) by $\alpha = n\sigma = \rho\kappa$. By differentiating Beer's law we can obtain the standard form for the attenuation of a ray passing through some absorbing media, i.e. radiative transfer equation for a non-emitting medium

$$\frac{dI_\nu}{ds} = -\alpha_\nu I_\nu \quad (4.1)$$

where intensity and absorption can be frequency dependant. This absorption can also incorporate scattering processes, as well as standard photon thermalisation. The optical depth can then be defined as¹

$$\tau_\nu = \int_{s_0}^{s_1} \alpha_\nu ds \quad (4.2)$$

where significant absorption (of order e) will occur for optical depths of order 1, where the medium is referred to as *optically thick*. The medium can also be allowed to emit additional radiation as the incident ray passes through, contributing further to the total radiation intensity quantified by an emission co-efficient j_ν with units² [$\text{erg s}^{-1} \text{cm}^{-3} \text{Hz}^{-1} \text{ster}^{-1}$] which can similarly be related to a density independent emissivity, ϵ_ν , by $j_\nu = \rho\epsilon$. This changes Equation 4.1 to the full radiative transfer equation for an absorbing and emitting medium

$$\frac{dI_\nu}{ds} = j_\nu - \alpha_\nu I_\nu. \quad (4.3)$$

It is then prudent to define the source function, the ratio of emission to absorption processes,

¹This is the same optical depth as used in the shielding processes incorporated in the cooling and chemistry in Chapter 2.

²These are the also the units of the ray intensity due to the definition of intensity as the energy emitted per unit area, per solid angle, per second, per unit frequency, i.e. $dE = I_\nu dA d\Omega d\nu dt$.

simply given by:

$$S_\nu = \frac{\epsilon_\nu}{\kappa_\nu} \equiv \frac{j_\nu}{\alpha_\nu} \quad (4.4)$$

which means we can re-cast Equation 4.3 as

$$\frac{dI_\nu}{d\tau_\nu} = S_\nu - I_\nu. \quad (4.5)$$

The solution to which can be found by multiplying through by e^{τ_ν} , grouping all I_ν terms into $d(I_\nu e^{\tau_\nu})/d\tau$ and then integrating from $\tau_\nu = 0$ (the initial ray position) to τ_ν to give the full solution as:

$$I_\nu(\tau_\nu) = I_\nu(0)e^{-\tau_\nu} + \int_0^{\tau_\nu} S_\nu(\tau'_\nu)e^{-(\tau_\nu-\tau'_\nu)}d\tau'_\nu \quad (4.6)$$

where $I_\nu(0)$ is the incident intensity, and $I_\nu(\tau_\nu)$ the emerging intensity after attenuation through an optical depth τ_ν (Rybicki & Lightman 1979). If the source function is constant along the path of the ray (e.g. the temperature in the medium is constant) then the integral can easily be evaluated as

$$I_\nu(\tau_\nu) = I_\nu(0)e^{-\tau_\nu} + S_\nu(1 - e^{-\tau_\nu}) \quad (4.7)$$

in which the first term on the right hand side encompasses emission entering the medium and being attenuated by absorption, while the second term is the emission from within the medium, that is also being attenuated by the medium itself. In the optically thin limit ($\tau \ll 1$), this becomes $I_\nu(\tau_\nu) = I_\nu(0) + ds(j_\nu - \alpha I_\nu(0)) \approx I_\nu(0) + j_\nu ds$, and the incoming radiation only receives positive contributions from the medium. In the optically thick regime ($\tau \gg 1$) this reduces to $I_\nu(\tau_\nu) = S_\nu$, with all the incident radiation being absorbed and the only contribution to the emerging ray coming from that emitted by the medium and not instantaneously absorbed.

The form of the source function depends on the physics of the medium in question. In complete thermal equilibrium there is no change in ray intensity, and so the source function is simply the radiation intensity, $S_\nu = I_\nu$. If thermal equilibrium is in effect then by Kirchoff's law the intensity is simply given by the Planck function, i.e. that of a black body, $I_\nu = S_\nu = B_\nu(T) = j_\nu/\alpha_\nu$. The relation between source and Planck functions not only holds in full thermodynamic equilibrium, but local thermodynamical equilibrium also (LTE) where $I_\nu \neq S_\nu = B_\nu(T)$. If intensity increases in passage through the medium then $dI_\nu/d\tau_\nu > 0$ and $B_\nu > I_\nu$, conversely if intensity decreases $dI_\nu/d\tau_\nu < 0$ and $B_\nu < I_\nu$ (Böhm-Vitense 1989). In LTE calculations the level populations required for transitions are purely a function of temperature, and collisional thermodynamical rates dominate the energy transport. In non-LTE the radiation field rates dominate the collisional rates, and the source function is no longer purely a result of black body emission.

We now turn to the determination of the emissivity and opacity for each of the two transitions of interest. These are the HI 21cm hyperfine transition, and the CO roto-vibrational $J = (0 \rightarrow 1)$ 2.6mm transition (see Sec. 1.4). The terms do not share the same formalism due to the different physical process underlying each transition. Beginning with the hydrogen line and the definition of emissivity as

$$j_\nu = \frac{h\nu_0}{4\pi} A_{ul} n_u \phi(\nu) \quad (4.8)$$

where the spin-flip hyperfine transition has an Einstein co-efficient of spontaneous emission of $A_{\text{HI}(21\text{cm})} = 2.9 \times 10^{-15} \text{s}^{-1}$ and a wavelength ($\lambda_0 = c/\nu_0$) of 21cm, making the transition temperature between the upper and lower levels, u and l , $T_{ul} = 0.068\text{K}$ (Binney & Merrifield 1998). $\phi(\nu)$ is the line profile function, discussed later in this section. The occupancy of states will determine the number density of the upper state; n_u . This can be determined from the Boltzmann equation

$$\frac{n_u}{\sum_i n_i} = \frac{g_u e^{-E_u/k_B T}}{Z(T)} \quad (4.9)$$

where the partition function is given by $Z = \sum_i g_i e^{-E_i/k_B T}$, a property of the system and solely a function of T , and g_i is the statistical weight of the i^{th} level. By equating partition functions and taking rates of the upper and lower levels of the transition we get the relation

$$\frac{n_u}{n_l} = \frac{g_u}{g_l} e^{-(E_u - E_l)/k_B T}. \quad (4.10)$$

The value $(E_u - E_l)/k_B$ is equivalent to T_{ul} . In every case the temperature of the medium will be greater than or equal to that of the CMB (2.73K), so $T \gg T_{ul}$ and so reducing the exponential above to unity. As the 21cm line is a spin-flip transition the degeneracy of states is simply $g = 2S + 1$, where $S = 0$ or 1 and so $g_l = 1$ and $g_u = 3$. This makes the ratio of state number densities $n_u = 3n_l$, and $n_u = 3n_H/4$, where n_H is the total number density of hydrogen. This results in an emissivity that can be expressed from Equation 4.8 as (Acreman et al. 2010a):

$$j_\nu = \frac{3\nu_0 h A_{\text{HI}(21\text{cm})}}{16\pi} n_H \phi(\nu). \quad (4.11)$$

By using the assumption of LTE and Kirchoff's law ($S_\nu = B_\nu = j_\nu/\alpha_\nu$) the opacity can easily be calculated. The Rayleigh-Jeans approximation reduces the Planck function to only the tail of the black body distribution, and is valid where thermal energy is much greater than that of the transition (such as radio astronomy) and $k_B T \gg h\nu$. This reduces the Planck function to

$$B_\nu(T) = \frac{2h\nu^3}{c^2 \left(\exp\left[\frac{h\nu}{k_B T}\right] - 1 \right)} \approx \frac{2k_B T \nu^2}{c^2} \quad (4.12)$$

giving an opacity for the hydrogen line of

$$\alpha_\nu = \frac{3c^2 h A_0}{32\pi k_B \nu_0} \frac{n_H}{T} \phi(\nu). \quad (4.13)$$

For the molecular CO transition the temperature of the transition is 5.53K, which is comparable to ISM temperatures so that the simplifications made above for HI no longer hold. The opacity is defined in full by the Einstein coefficients of stimulated emission (B_{ul}) and stimulated absorption (B_{lu}):

$$\alpha_\nu = \frac{h\nu_0}{4\pi} (n_l B_{lu} - n_u B_{ul}) \phi(\nu) \quad (4.14)$$

for a transition from u to l , and the emissivity is again given by Equation 4.8. This reduces the source function to simply $A_{ul} n_u / (n_l B_{lu} - n_u B_{ul})$. To solve the radiative transfer equation the line

profile is still needed in the opacity, determined from Equation 4.14. The Einstein A co-efficient for this transition is $A_{\text{CO}(0 \rightarrow 1)} = 7.2 \times 10^{-8} \text{s}^{-1}$ (Schöier et al. 2005) from which the B coefficients can also be calculated³. The population of states is given by Equation 4.10 where the degeneracies of the upper and lower states are 1 and 3 respectively ($g = 2J + 1$), providing everything required to calculate the emissivity and opacity of the CO and HI transitions of interest. The above expressions are only valid in LTE where the level populations can be calculated by Boltzmann statistics. In LTE level populations are calculated from local temperature alone where the density is sufficiently high that thermal collisions dominate radiative effects. In non-LTE regions the level populations are calculated by assuming statistical equilibrium between states and must be iteratively solved for, including the effect of the global radiation field (i.e. n_u is a function of I_ν). This makes the calculation exceedingly more complicated and time-consuming. The calculations performed within this thesis assume LTE, which should hold in the dense cold regions of the ISM where CO emission originates. Non-LTE effects become important in diffuse regions where radiative effects dominate (e.g. stellar coronae, see Rundle et al. 2010 for an application).

The final ingredient of the radiative transfer equation is the profile function, ϕ_ν , which contains the velocity information of the medium. For the ISM thermal broadening is the dominant effect, for which the profile takes a Gaussian form

$$\phi_\nu = \frac{c}{v_b v_0 \sqrt{\pi}} \exp\left(-\Delta\nu^2/v_b^2\right) [\text{cm}^{-1}] \quad (4.15)$$

where v_b is the broadening width given by a combination of thermal (v_T) and turbulent (v_{turb}) effects as $v_b^2 = v_T^2 + v_{\text{turb}}^2$ where $v_T = \sqrt{Tk_B/m}$. The turbulent velocity is a collection of any velocity structure not included in the global velocity field resolved by the calculation, e.g. supernovae feedback, stochastic gas motion, and MHD effects, which can be of the order of km s^{-1} (Larson 1981). Other broadening processes include pressure and natural broadening which take the form of a Lorentzian profile but become important in extremely different environments such as planetary atmospheres. The velocity of the gas (v) is incorporated in the Doppler shift of the rest frequency,

$$\Delta\nu = (v - v_0) \frac{c}{v_0} + \vec{v} \cdot \hat{n} \quad (4.16)$$

where ν is the frequency of the ray being traced. \vec{v} is the velocity field of the gas causing the absorption/emission and \hat{n} is the unit vector defining the direction of ray propagation (Rundle et al. 2010).

4.3 Creating l - ν maps and quantifying the best fit

The 3D AMR Monte-Carlo radiative transfer code `TORUS` (Harries 2000) is used to create synthetic observations, using the formulae outlined above. `TORUS` is capable of creating synthetic brightness temperature, T_B , data cubes (data structures with dimensions l, b, ν and T_B) enabling us to compare our simulations directly with the map of Dame et al. (2001). `TORUS` has been employed in several studies already to create synthetic emission from SPH simulations including star formation regions

³The Einstein coefficients are related by the relations $B_{ul}g_u = B_{lu}g_l$ and $A_{ul} = B_{ul}2h\nu^3/c^2$.

(Rundle et al. 2010) and circumstellar discs (Acreman et al. 2010b). Synthetic HI maps of the spiral galaxies of M31 and M33 were created by Acreman et al. (2010a), finding good agreement with observed emission. Douglas et al. (2010) and Acreman et al. (2012) also used `TORUS` to create synthetic emission maps of the second quadrant of our Galaxy from SPH calculations in HI.

The procedure to create l - b - v data cubes, analogous to those created from observations, is described in detail in Acreman et al. (2010a) and we will give only a brief description here. Creation of synthetic observations is a two stage process. An AMR grid is first generated, containing all the data required for the radiative transfer calculation, through which the actual ray-trace can then be performed. The SPH data must first be converted to a grid for use by `TORUS`. This is done using the method of Rundle et al. (2010). A grid is constructed with SPH particles using an octree method, where the grid is initially a $2 \times 2 \times 2$ cube. The grid is then subdivided according to a mass per unit cell criterion, thereby providing greater refinement in regions of high particle concentration. Our grid is somewhat larger than previous works of Douglas et al. (2010) and Acreman et al. (2012) that focused on the second quadrant alone. As such, to make the grid manageable in terms of memory and map construction time we use a higher mass per unit cell of $4 \times 10^4 M_\odot$ where each particle has a mass of $1.6 \times 10^3 M_\odot$, giving approximately 25 particles per cell. This results in approximately half a million splits by mass (around 4 million voxels) and a full galactic grid over 6GB in size. We find that higher mass thresholds (lower resolution) have very minimal effects on the resulting l - v maps, merely reducing the arm resolution slightly. The grid to SPH conversion is illustrated by Figure 4.1 where we show an SPH input file and the equivalent AMR grid, along with cell boundary and particle positions. The SPH particle properties including HI and CO number densities, temperature and velocities are mapped onto the grid using a summation of SPH kernels with a Gaussian form. The opacity and emissivity, assuming LTE, are then calculated and stored in the AMR grid for use in the radiative transfer ray-tracing.

The ray-trace is then performed with input values for the observer co-ordinates, requiring the distance from the Galactic centre, R_{obs} , the azimuthal position in the disc, l_{obs} and the circular velocity, V_{obs} . For a certain velocity channel rays are propagated from the observer throughout the disc in a range of $0^\circ < l < 360^\circ$ and $|b| < 6^\circ$. While out of plane emission is of minor importance for studying the Galactic disc, we pass rays out of the plane in a high enough latitude so we can produce an integrated emission map of comparable strength to that of Dame et al. (2001). As a ray enters a cell the intensity of emission is updated from I_ν to I'_ν using the opacity, emissivity and optical depth of the current cell at the frequency of interest ν (ϵ_ν , κ_ν and $d\tau$ respectively) via Equation 4.7 allowing for the optically thick or thin treatment of the transition. The actual quantities stored by the grid are independent of the velocity profile function, which is instead applied during the ray trace itself.

The intensity is transformed into brightness temperature by using the Rayleigh-Jeans approximation (Equation 4.12 with $I_\nu = B_\nu$). This process is then repeated for each velocity channel of interest, resulting in a cube of T_B as a function l , b and v_{los} . The resulting data cube is then integrated over the latitude dimension ($|b| < 2^\circ$) to produce an l - v map analogous to that in Dame et al. (2001). The number of velocity channels is considerably higher in the central galaxy in order to encompass emission up to a maximum of 280 km s^{-1} seen in the CO observations. To

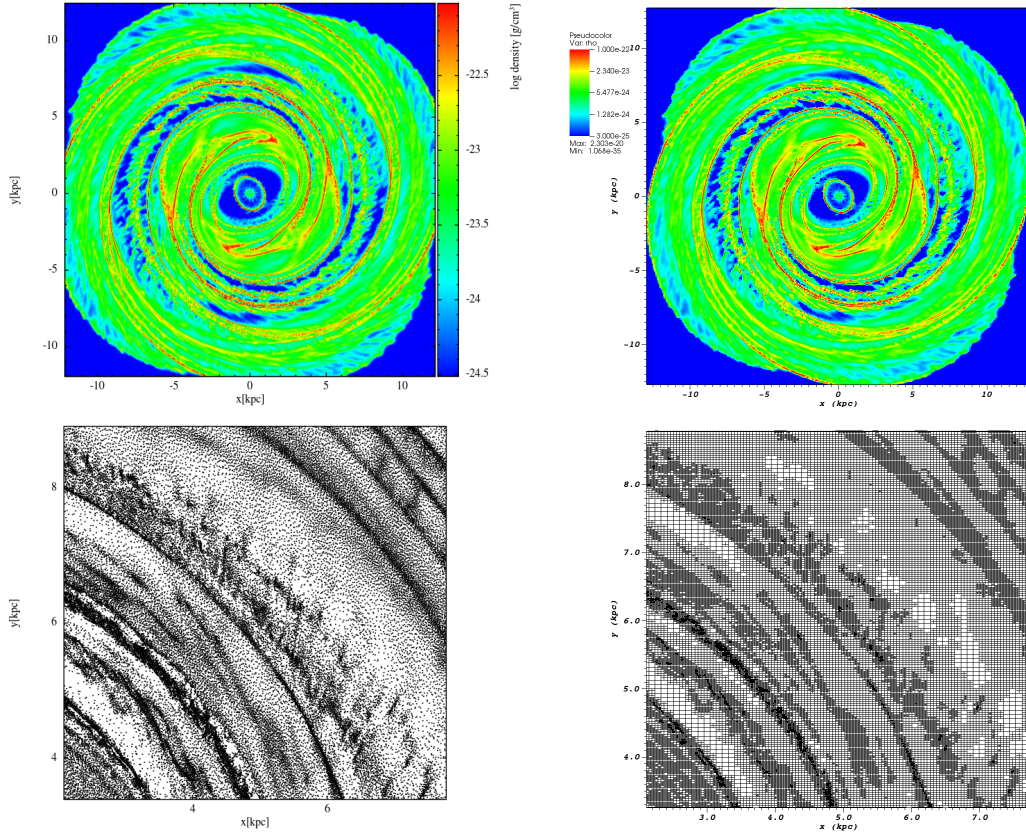


Figure 4.1: Illustration of the SPH to AMR grid conversion. Left column shows the SPH data (density render top, SPH particles bottom), and the right the AMR grid (density render top, grid cell boundaries bottom). The lower panels show a zoom in on the second quadrant and the upper panels the full barred-spiral galaxy density render.

avoid passing rays through empty regions of l - v space we use a number of channels that varies as a function of longitude, tailored to encompass the emission seen in Dame et al. (2001). As the HI emission spans a greater region of l - v space the datacube is simply cut-through at $b = 0^\circ$ rather than integrated. The integration version of the observed HI emission adds little to the l - v structure, whereas the CO features show additional features upon integration. Though the CO integration usually does not introduce any new features in l - v space as our simulations are effectively confined to the Galactic plane.

A fit statistic is calculated for each resulting map to quantify similarity to observed emission. The statistic used is the same as Equation 3.20 for the simple kinematic l - v maps. The TORUS map tends to be of finer resolution than the relatively coarse Dame CO map, so is first rebinned to a lower resolution, after being smoothed in longitude slightly to provide a smoothness of the resolution of the Dame map. Our primary interest is whether emission features can be produced in the same location in l - v space, with comparable arm to inter-arm emission strengths. As such we are not so interested in the quantitative strength of the emission itself. As is discussed in greater detail below, the strength of the torus CO emission is somewhat higher than that in observations, with peak emission features approximately double the strength. To ensure the fit

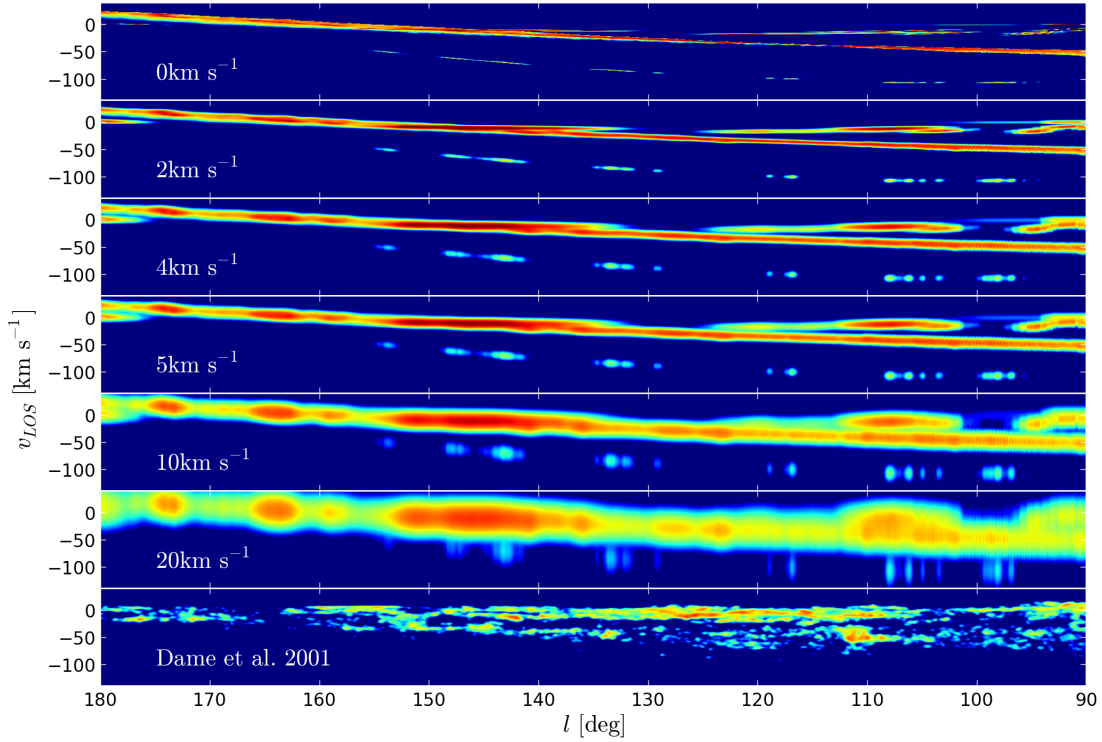


Figure 4.2: CO emission maps of the second quadrant in CO in a spiral galaxy with the galaxy aligned so arm features are located in the l - v space in a similar position to the Local and Perseus arms in observations (bottom panel). Each panel shows calculations with varying turbulent velocity contributions in Equation 4.15.

is not driven too much by this difference each map is scaled to have emission that matches that of the Dame map for the calculation of a fit statistic, which effectively halves the strength of CO emission. All plotted TORUS l - v maps retain their original strength.

4.4 General features of RT maps

Early tests using TORUS for CO l - v maps showed that the features created were far too narrow in velocity width compared to observations. Figure 4.2 shows CO emission from the second quadrant in an armed galaxy simulation with various turbulent velocity contributions ranging from 0-20 km s^{-1} . The map with no turbulent velocity has features much finer than those seen in observations (bottom panel). To resolve this we added a turbulent velocity to the width of the CO line emission profile of 4 km s^{-1} , a value high enough to smear out the fine emission features but not so strong as to blend features in l - v space. This is at the lower end of ranges suggested by CO observations of the outer regions of disc galaxies (see Dib et al. 2006 and references therein). The turbulent velocity could be scaled as a function of some cloud size determined by the clumpiness of SPH particles (Larson 1981; Dame et al. 1986; Brunt et al. 2003; Mac Low & Klessen 2004). However, we choose a constant factor to avoid introducing additional variables.

In Figure 4.3 we show full galactic plane l - v maps for HI and CO emission for calculations with varying surface density (i.e. total SPH particle gas mass), increasing from bottom to top. The CO emission is very strongly coupled to the disc mass, with emission features appearing

extremely weak in the lowest surface density case. With a low surface density the SPH particles are not massive enough to enter the upper region of the $n - \chi_{\text{CO}}$ diagram (Fig. 2.14), and stay relatively warm throughout the simulation. The two higher surface density calculations show CO emission that appears to trace arm and bar features, though still appear too weak in the $7.5M_{\odot}\text{pc}^{-2}$ case compared to observations. The highest surface density calculation was deemed as having a high enough mass to have visible $l-v$ emission features in CO, and so was the mass adopted in the highest resolution models used in this and the previous chapter.

While the structure of the HI emission is not the prime goal of this work, as it is not believed to trace high density structures as well as molecular gas, emission maps were also created of the entire Galactic plane with varying surface density, similar to those shown in Acreman et al. (2012). The features seen are quite different to those shown in the CO emission. The HI emission only seems to trace the high density regions associated with arms and bars in the lower surface density cases (lower two panels). In the calculations with higher surface densities there appears to be an equal amount of emission coming from the inter-arm regions as the arms themselves, if not more. A possible explanation for this is that the gas in simulations shown here is very confined to the x - y plane, as there is no mechanism to drive the gas off-plane and counteract the disc potential. This causes all the ISM material to be within a single latitude channel in the construction of the emission data cubes. This would cause the optical depth of the atomic gas to be very high in the $b \approx 0^{\circ}$ channels, especially in the highest surface density case. As such the high densities, and therefore high optical depths, of the HI in the arms can result in a net loss of emission, explaining why the arm features in the highest surface density HI map in Figure 4.3 seem to show dearth of emission compared to that with the lowest surface density. The reason this was not seen in the work of Acreman et al. (2012) is that their surface density was somewhat lower, corresponding with the lower panels of Figure 4.3, where the HI does trace arm structure. Stellar feedback was also included in those models, acting to drive material off-plane. The earlier calculations of Douglas et al. (2010) are similar to those shown here. There is a considerable amount of off-plane emission seen in observations (Grabelsky et al. 1987; Bloemen et al. 1990; Dame et al. 2001), so it may be that our axisymmetric model is too strong in the vertical direction, though this would lessen the amount of molecular gas due to the drop in density, and weaken the CO emission structures.

It may be the case that there is some careful balance required to having a high enough surface density to produce CO emission, but not too high to create adverse absorption in HI. There is also the possibility that the chemistry is too simplistic to allow the accurate modelling of HI and CO. To test the effects of the optical depth on the HI emission we performed calculations where the atomic and molecular gas was assumed to be optically thin. The calculation was performed by simply adjusting Equation 4.7 to instead read $I_{\nu}(\tau_{\nu}) = I_{\nu}(0) + j_{\nu}ds$ for both the atomic and molecular ray-trace. Figure 4.4 shows HI and CO emission for the optically thin case from the second quadrant alone, using the same SPH input as Figure 4.3. In this case both the atomic and molecular gas appears to trace the arm structures. The differences in CO emission are much less apparent than in HI, but there is a minor change in emission strength. The peak HI emission is much stronger than in the optically thick cases, reaching temperatures above 1000K, which far exceeds that of the optically thick calculation and temperatures seen in observations. This indicates

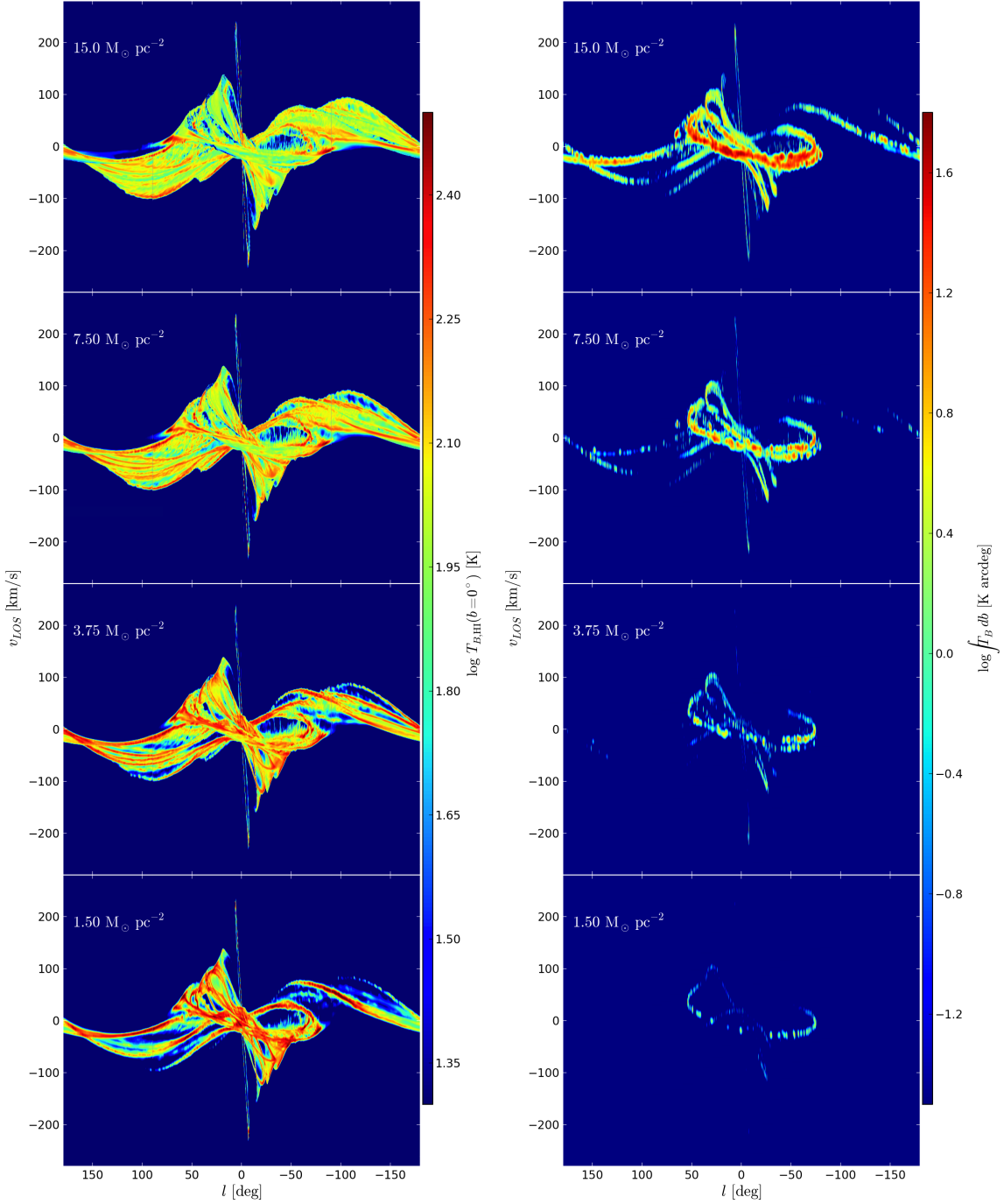


Figure 4.3: HI (left) and CO (right) emission maps of barred-spiral galaxies of similar morphologies to that in Fig. 4.1 with varying surface densities, increasing from bottom. The corresponding total gas mass is $8, 4, 2,$ and $0.8 \times 10^9 M_\odot$ from top to bottom. The potentials and observer location are the same in all maps, with the observer placed at $R_{\text{obs}} = 8 \text{ kpc}$.

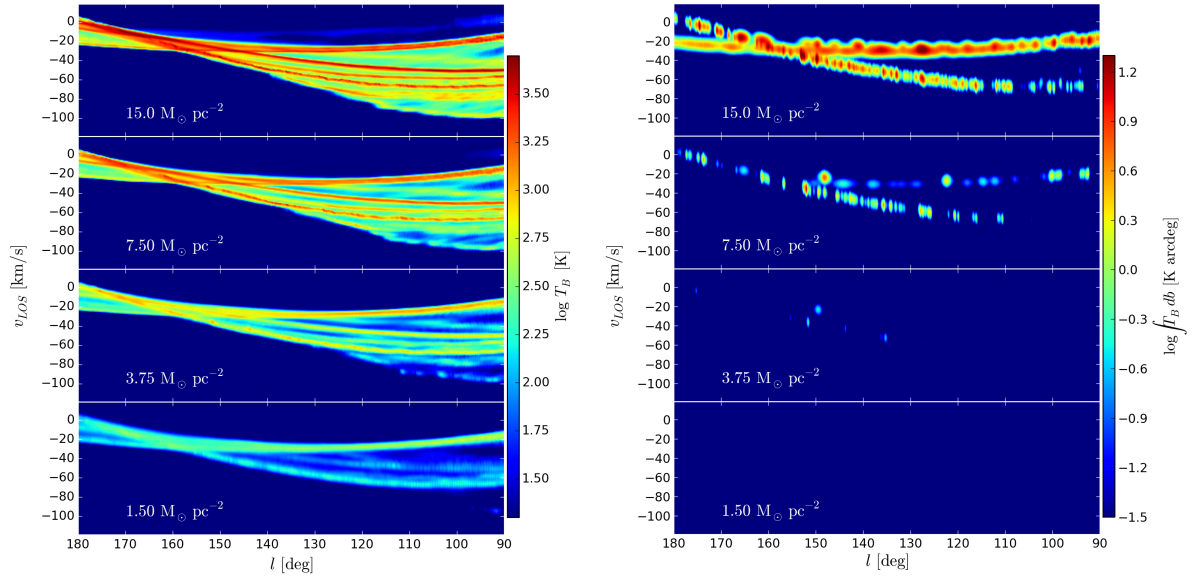


Figure 4.4: The same maps as Fig. 4.3 except in the optically thin regime with negligible optical depth, and only of the second quadrant. HI emission is shown in the left panel, and CO in the right panel in calculations with varying surface density.

that the HI does also trace arm structures, but that the absorption is too high in our standard calculations. Without such a high density however, CO production will be too low, and so we believe that correctly modelling the atomic and molecular emission simultaneously is not possible with the chemistry and potentials used here. Additional physics or more complex chemistry would be needed to break up the atomic gas and reduce its opacity while allowing for sufficient CO production to produce observable emission features.

The contrast between CO emission in our TORUS maps is comparable to that of the observations in the inner Galaxy when a 4 km s^{-1} turbulent velocity is added. The distribution of emission in general is smoother than that seen in observations. This is a result of the continuous nature of the potentials, which are idealised compared to the arm structures in observed spiral galaxies. Inclusion of other physical processes, such feedback as in Acreman et al. (2012) or a live stellar component as in the following chapter, will act to break up these smooth l - v features.

The strength of the CO emission in our TORUS maps is somewhat higher than that observed, peaking at approximately 40K compared to 20K seen in observations in the highest surface density case. The peak emission in the second highest density calculation is in closer agreement with observations, but arm features appear much weaker in comparison. There are several possible reasons for this difference. The first is that the strength of the CO emission is very sensitive to the surface density of the ISM disc. The disc mass found through integration of the disc surface density profile resulted in visible emission from the arm features, and so was used for the majority of the simulations presented here. Another consideration is that the production of CO has no limit other than the maximum amount of C allowed to be present in the ISM. All SPH particles tend to increase their molecular abundance (and density) up to this limit, as there is no strong process to break up and heat the gas. Additional heating mechanisms such as stellar feedback or magnetic

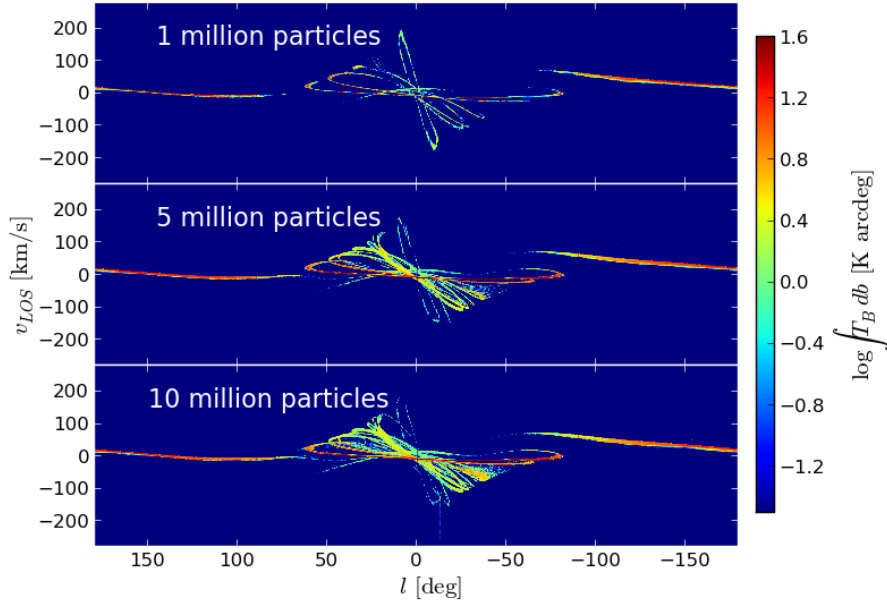


Figure 4.5: Radiative transfer CO l - v maps resulting from an SPH simulation with 1, 5 and 10 million particles (increasing from top). The gas is subject to a bar potential moving at $40 \text{ km s}^{-1} \text{ kpc}^{-1}$, shown after 280 Myrs of evolution. The observer is set to the IAU standard position and velocity. Turbulent velocity broadening is excluded to highlight differences between different resolutions.

fields would be required to break up the dense clumps of ISM gas and remove some of the excess CO build up. The addition of stellar feedback would also cause material to be more dispersed vertically compared to the no feedback case (Tasker & Bryan 2006; Dobbs et al. 2011; Acreman et al. 2012). The confinement of the gas to the x - y plane may also cause this over-emission. The molecular material will be located in a single latitude channel in the construction of the emission data cubes, increasing the strength of emission seen in l - v space, but the amount of the molecular material still being low enough to not have a large absorption effect.

4.4.1 Resolution study

To test our adopted simulation resolution of 5 million particles we ran a number of simulations with 1 and 10 million particles. Top down maps of 1 million particles displayed significantly less structure around the resonance regions of the potentials, while 5 and 10 million particle calculations showed little difference. Figure 4.5 shows CO l - v emission maps made using `TORUS` for simulations using 1, 5 and 10 million particles (increasing from top) inside a bar potential. No turbulent velocity term is added to the line profiles so as to highlight the resolution effects. The difference between 5 and 10 million particles appears to be minimal, but the 1 million run has considerably less emission in the inner Galaxy in comparison. We conclude the 5 million particle resolution is sufficient to capture the global Galactic CO emission.

The 1 million particle resolution calculations have a much lower CO formation efficiency, with a very low molecular gas fraction compared to the higher resolutions. They will cause weaker CO emission which, coupled with the weaker tracing of potentials in low resolution runs, causes

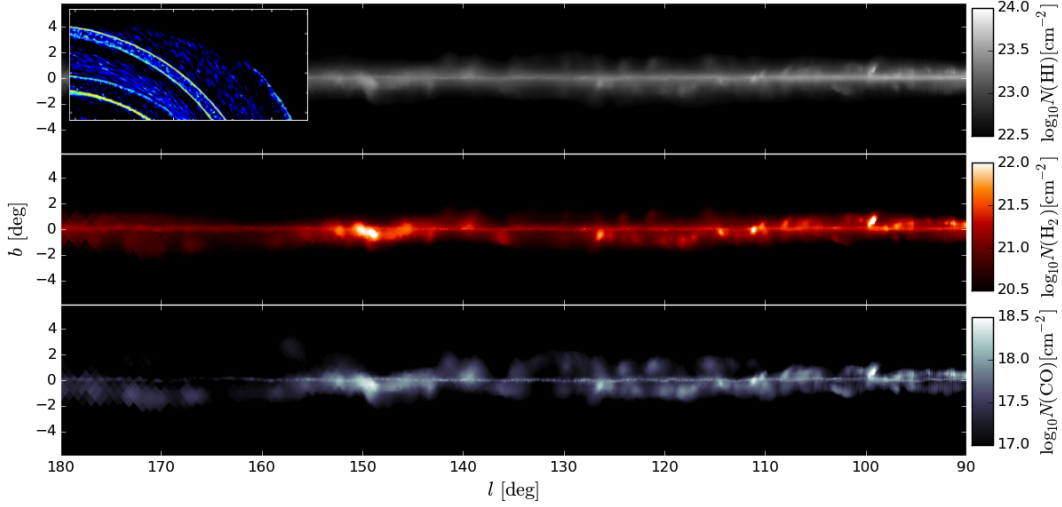


Figure 4.6: Column density of HI (top), H₂ (middle) and CO (bottom) of the second quadrant of a simulation with a spiral perturbation, shown in the insert.

the observable decrease in CO emission features seen in Figure 4.5.

4.4.2 ISM Column densities

The column density of the gas is an important quantity for both the radiative transfer and the ISM chemistry. Figure 4.6 shows the column density of the second quadrant of a spiral galaxy simulation (pictured in the top left corner). The column density of the atomic hydrogen, molecular hydrogen and CO gas is shown in the top, middle and bottom panels respectively, as a function of longitude and latitude. Firstly, it is clear that the column density (and therefore opacity) is decreasing with mass of the ISM species in question, due to the decreased abundance of each species in the simulation. There are two major arm segments in this quadrant seen in the insert, both of which can be seen in the column densities. The molecular gas (both H₂ and CO) is primarily confined to higher density regions associated with spiral arms. In the corresponding column densities a far and near arm structure can be seen. The far arm is confined to the $b \approx 0^\circ$ plane due to its relatively large distance from the observer, while the near arm appears as the off plane clumps that span a wide range of latitudes due to their closer proximity. The atomic gas however has a weaker affinity to these arm features, especially compared to CO, seen throughout the plane.

In Figures 4.7 we show the column density of HI and CO for the entire Galactic plane of the same barred-spiral calculation as that used in Figure 4.1. Here an even clearer distinction between the atomic and molecular gas column density distribution can be seen. The HI column density is not only predominantly confined to the mid-plane, but also present at all longitudes. There is some off-plane emission in the inner disc where the bar is causing turbulent gas motions relatively close to the observer's location, but the column density is still relatively thinner than that in-plane. Conversely, the CO is much less uniformly distributed through longitude. The third quadrant in

particular has a very low column density compared to the inner quadrants. The off-plane density associated with arm/bar structure is also closer to that of the in-plane density than the HI.

Figure 4.7 shows some numerical artefacts of the SPH to grid conversion. The local material that has a relatively large angular size clearly shows cube-like features inherent to the grid based nature of the ray-trace. These features can be muted by decreasing the mass per units cell criterion, though this will further increase the already hefty memory requirements of the AMR grid. This will only help so much however, and in order to fully remove these artefacts the resolution of both the SPH calculation and the AMR grid must be increased. The effect of this numerical artefact is seemingly unimportant in the CO l - v maps, where the emission is integrated through latitude. This was tested by performing calculations with lower values of the mass per unit cell parameter, and the resulting l - v emission maps showed no visible change.

In Figure 4.8 the column density of H₂ and CO is shown for a Galactic simulations after 120Myrs and 340Myrs of evolution in the left and right panels. Column densities from several other works in the literature are also plotted as coloured circles, including data from Sheffer et al. (2008); Burgh et al. (2007); Ungerer et al. (1985); Baudry et al. (1981) and Federman et al. (1980). The figure also includes a line indicating the maximum CO column density allowed by formation from H₂ (Sheffer et al. 2008). The earlier time-frame shows column densities that agree with those of moderately diffuse molecular clouds, but not of the denser cores of Ungerer et al. (1985) and Baudry et al. (1981). The global trend does not match that seen in observations. The column densities in our calculations appear to drop away $N(\text{H}_2) < 10^{19}\text{cm}^{-2}$, following an inverse exponential profile. Observations on the other hand appear to have a near constant $N(\text{CO}) \approx 10^{12}\text{cm}^{-2}$ when $N(\text{H}_2) < 10^{19}\text{cm}^{-2}$, though there are much fewer data in this region, and the data appear to follow a quadratic profile. The densities at the later time agree much better with the higher density molecular clouds, but produces too high values of $N(\text{CO})$ for the more diffuse clouds. This later time frame is much closer to that used for construction of l - v maps, thus at that time it is assumed that we are correctly reproducing the molecular column densities in the denser region of the ISM. We are however over-estimating the CO column densities for the more intermediate density clouds. This can result in excessive absorption of CO emission in some regions, but also reduced emission, as the column density is dependant of CO mass, which dictates the actual CO emission.

While we are not expecting to fully match the column densities of the ISM, the values in our calculations seem to agree well with those observed for the highest density regions. As these regions are the primary CO factories in our calculations it shows our chemical network underlying the CO emission maps matches some observed ISM properties. The lower column densities however likely need a better treatment of additional ISM physics. Our calculations are designed to resolve the colder ISM component rather than the warmer region where these lower column densities are seen. This region is also populated by very few data points compared to the well populated region that our calculations reproduce.

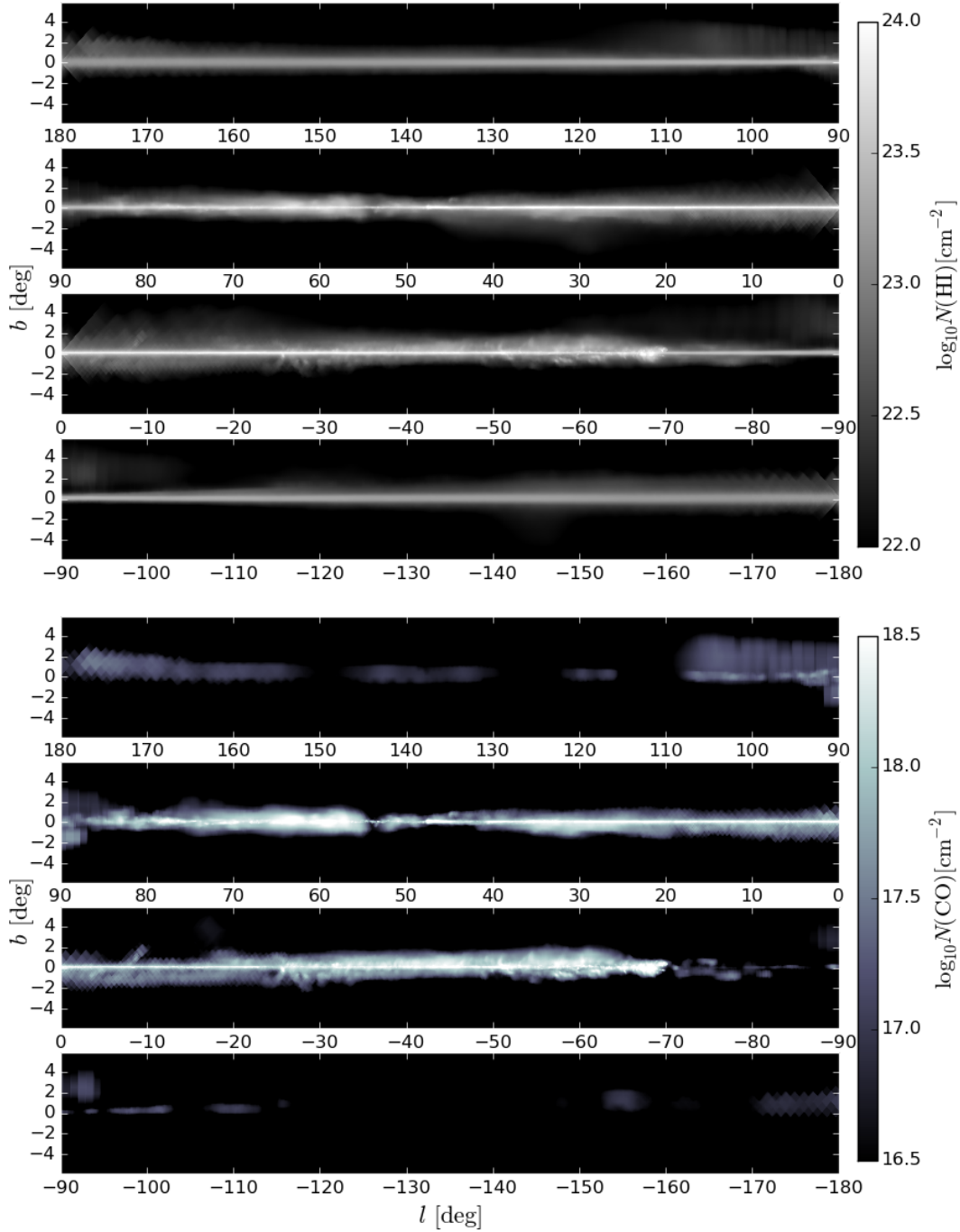


Figure 4.7: Column density of HI (top) and CO (bottom) of the entire Galactic plane for a barred-spiral calculation of similar morphology to that in Fig. 4.1. The four separate panels show the column density in each of the four Galactic quadrants.

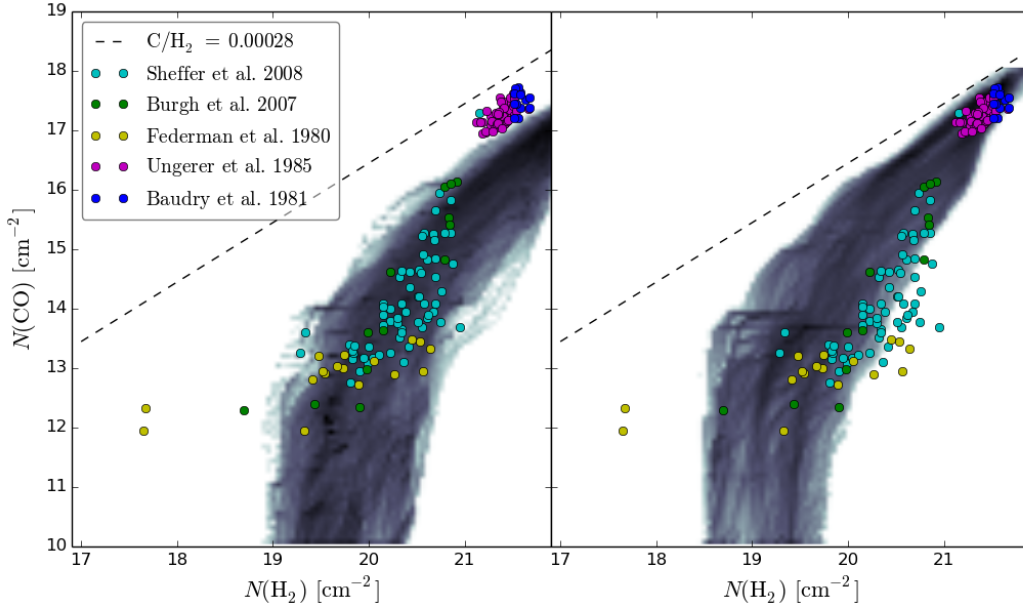


Figure 4.8: Column density of H_2 and CO for the second quadrant of a simulation with a spiral perturbation. The points show observational data from Sheffer et al. (2008); Burgh et al. (2007); Ungerer et al. (1985); Baudry et al. (1981) and Federman et al. (1980). The dashed line indicates the maximum CO column density allowed by formation from H_2 (Sheffer et al. 2008). Left and right panels show the calculation at 120Myrs and 340Myrs.

4.5 Radiative transfer maps of armed or barred simulations

Before considering barred-spiral models we first discuss a selection of maps made using `TORUS` of our models presented in Chapter 3. The SPH inputs to the `TORUS` calculations are the same as those for Figures 3.18 and 3.23 (5 million SPH particles, with a total gas mass of $8 \times 10^9 M_\odot$), using the same values for observer position and velocity. We show full radiative transfer maps for only a handful of these models due to the high computational cost of construction, and choose to use the radiative transfer to primarily differentiate between full models including bar and arm potentials.

In Figure 4.9 we show `TORUS` maps of the WK bar at pattern speeds of 40, 50 and $60 \text{ km s}^{-1} \text{ kpc}^{-1}$ after 354 Myrs of evolution. These correspond to the simple maps shown in the centre of Fig. 3.18. The arm feature near the Solar position in the $40 \text{ km s}^{-1} \text{ kpc}^{-1}$ model is visible as extremely bright emission in the top panel of Fig. 4.9. The strength of this emission far exceeds that seen in observations, and the arm appears uniformly bright, not just in a specific location. As the pattern speed increases, the emission covers a narrower range of longitudes, and increases the line-of-sight velocity of the central emission ridge. As with the simple maps from the previous chapter, there is little emission in the outer quadrants with these relatively fast rotating bars. The emission towards the Galactic centre ($|l| < 5$) with the greatest $|v_{los}|$ is a very clear feature in the observed CO emission; the CMZ. We find no such strong emission in our maps in Fig. 4.9. We do see some similar features to the peak velocity structures seen in observations in some of our maps in Fig. 3.18, but there is not enough CO produced to be seen in our `TORUS` maps. We discuss this further in Section 4.7.

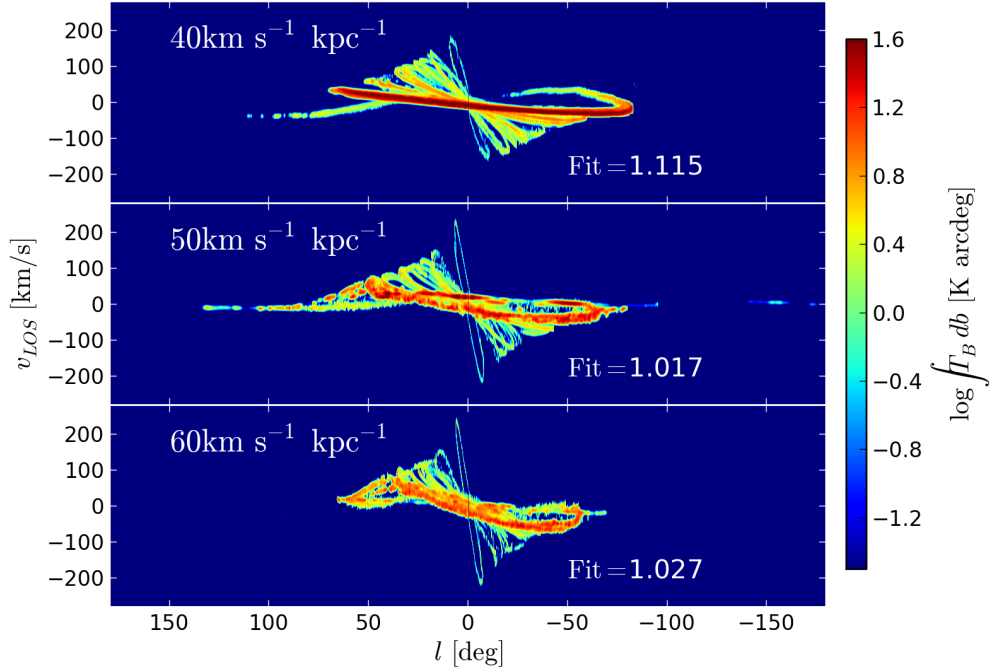


Figure 4.9: Radiative transfer l - v maps constructed using `TORUS`, rather than the simple chemokinematic re-mapping method used to create the maps in Fig. 3.18. The bar is that of Wada & Koda (2001) after 354 Myrs of evolution and pattern speeds of 40, 50, 60 $\text{km s}^{-1} \text{kpc}^{-1}$ (increasing from top to bottom). The brightness temperature scale is calculated exactly so the fit statistic is on a different scale to that for the previous maps.

Figure 4.10 shows a selection of 6 of the best fitting arm models made using `TORUS`, each with a different combination of N , α and Ω_{sp} . The $N = 2$ models cover a reduced area of l - v space compared to their $N = 4$ counterparts. This allows for $N = 2$ models to match emission in the 2nd quadrant while leaving the 3rd comparatively empty. This is seen in observations of CO, where possible arm features are much weaker in the 3rd quadrant compared to the 4th. The $N = 2$ models tend to have the near arm aligned with the Perseus arm feature in the 2nd quadrant and this arm reaches the edge of the disc just as it enters the 3rd quadrant. The local emission in the 2nd quadrant is reproduced by branches, whereas in the 4-arm models this is reproduced by arms directly tracing the potential troughs (as seen in the top panels of Fig. 3.22).

In the maps shown in Figures 4.9 and 4.10 there is little difference morphologically to the maps constructed in the previous chapter. Emission strength is similar to values seen in observations, though peak strengths are higher. There also appears to be a lack of weakly emitting material on the order of tenths of kelvin that appears to be present in both arm and inter-arm regions of observations. A full reproduction of all features in l - v space still seems impossible with only an arm or bar potential. Arms without the inclusion of a strong bar to drive additional features in the inner disc cannot allow the arms to produce the Carina and Perseus features in the outer quadrant without trying to fit the central ridge simultaneously. The placement of the OLR of the bar at roughly the Solar position would impact upon the structures observed in the 1st and 4th quadrants formed

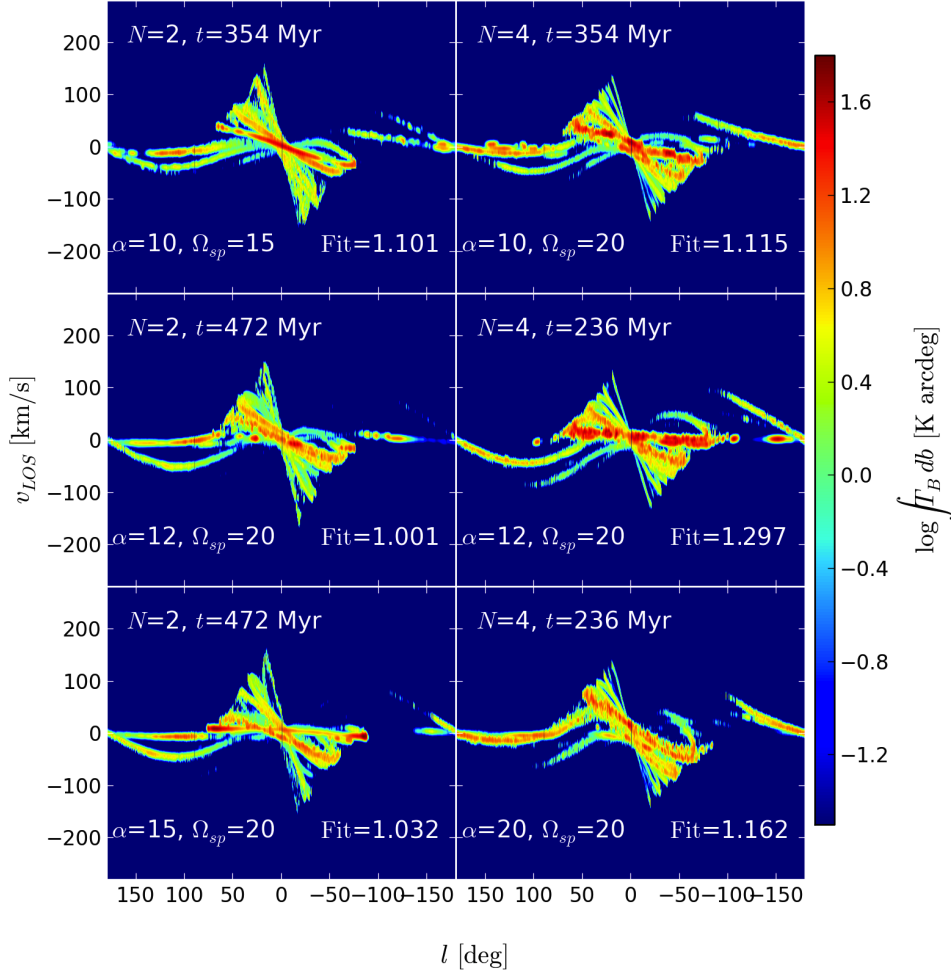


Figure 4.10: The best fitting maps from isolated arm potentials for a variety of pitch angles. l - v maps are made using the `TORUS` radiative transfer code, where the normalised fit to observed CO is shown in the bottom right of each panel. Ω_{sp} and α are in the units of $\text{km s}^{-1} \text{kpc}^{-1}$ and degrees respectively shown in the bottom left.

by the arms.

We also constructed CO l - v maps using `TORUS` of different arm models, including that of Cox & Gómez (2002) with double the fiducial strength and the arm model of Pichardo et al. (2004). The resulting maps did not differ significantly from the “simple” versions made in the previous chapter (Figure 3.29), and so confirmed our decision to not include these models in the barred-spiral models.

4.6 Simulations including both arm and bar potentials

Using the refined parameter space found from calculations with arm and bar potentials we then performed calculations with both in various combinations. In the following section we show the results of our simulations, simple map fitting to place the observer, and full radiative transfer calculations to create l - v emission maps, and determine the best-fitting morphology.

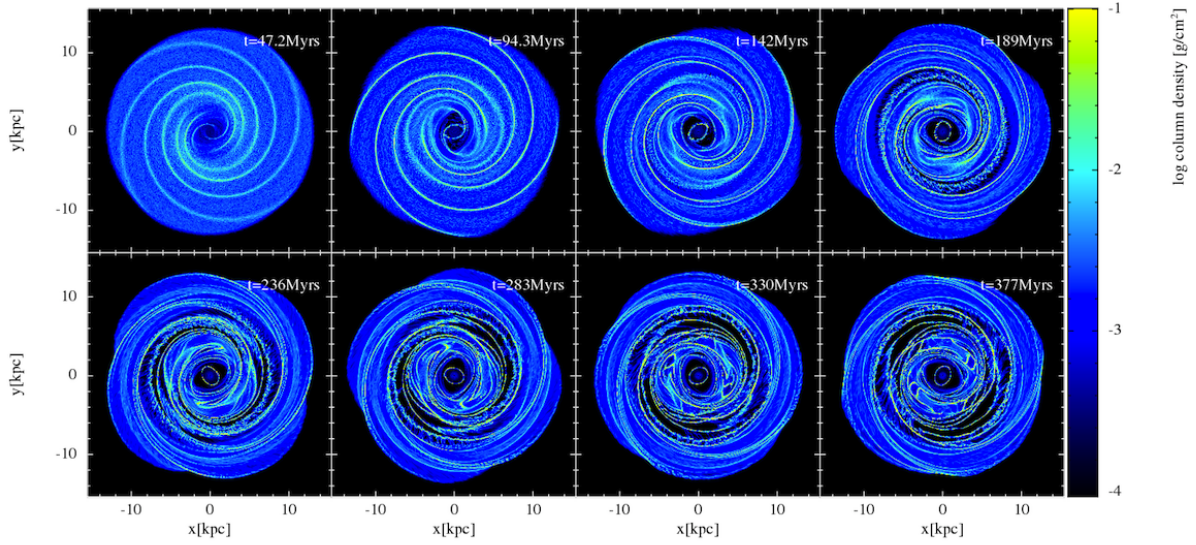


Figure 4.11: Example of the evolution of a barred-spiral Milky Way simulation. The central bar is of WK type with and the arms of CG type. The potential parameters are; $N = 4$, $\alpha = 12.5^\circ$, $\Omega_{sp} = 20 \text{ km s}^{-1} \text{ kpc}^{-1}$ and $\Omega_b = 50 \text{ km s}^{-1} \text{ kpc}^{-1}$.

4.6.1 Simulations

Parameters in bold in Table 3.2 are those used in arm-bar simulations, chosen based on fits in previous sections. Note that we use $\Omega_b = 50 \text{ km s}^{-1} \text{ kpc}^{-1}$ for the WK and $\Omega_b = 60 \text{ km s}^{-1} \text{ kpc}^{-1}$ for the WKr2 potentials. We use $\Omega_{sp} = 15 \text{ km s}^{-1} \text{ kpc}^{-1}$, $N = 2$ arms only in conjunction with the $\Omega_b = 60 \text{ km s}^{-1} \text{ kpc}^{-1}$ bar potential as the OLR of the $\Omega_b = 50 \text{ km s}^{-1} \text{ kpc}^{-1}$ bar is close to the region of arm branching and this may result in a disruption of these features. In some models resonances of arms and bars will overlap. For example, a $N = 4$ spiral at $\Omega_{sp} = 20 \text{ km s}^{-1} \text{ kpc}^{-1}$ and a bar with $\Omega_b = 50 \text{ km s}^{-1} \text{ kpc}^{-1}$ has the ILR of the arms at approximately the same radius as the OLR of the bar, so a clear distinction between arm and bar features should be seen in this model. This is not the case for the $N = 2$ models, where there will arm and bar features will overlap.

An example of the evolution of a barred-spiral simulation is shown in Figure 4.11, with the parameters; $N = 4$, $\alpha = 12.5^\circ$, $\Omega_{sp} = 20 \text{ km s}^{-1} \text{ kpc}^{-1}$ and $\Omega_b = 50 \text{ km s}^{-1} \text{ kpc}^{-1}$ (with CG and WK type potentials). The addition of a bar distorts the arm features within a radius of 5 kpc, roughly corresponding with the bar's OLR. The bar-arm contact region has a large amount of complex structure where the gas in the arm potential strays from a logarithmic spiral structure to join those arms driven by the bar; which are much tighter wound. After 500 Myrs the gas around the bar establishes elliptical orbits similar to those seen in Fig. 3.15, though the addition of arm potentials inhibits the formation of parallel and perpendicular elliptical orbits seen at the OLR in bar-only simulations. We find that, as suggested by Sellwood & Sparke (1988), there is a clear inner region dominated by the bar potential and outer region dominated by the spiral potential, with only a small region where the two are intermixed.

The differences between the models as a function of Ω_b and N are shown in Figure 4.12.

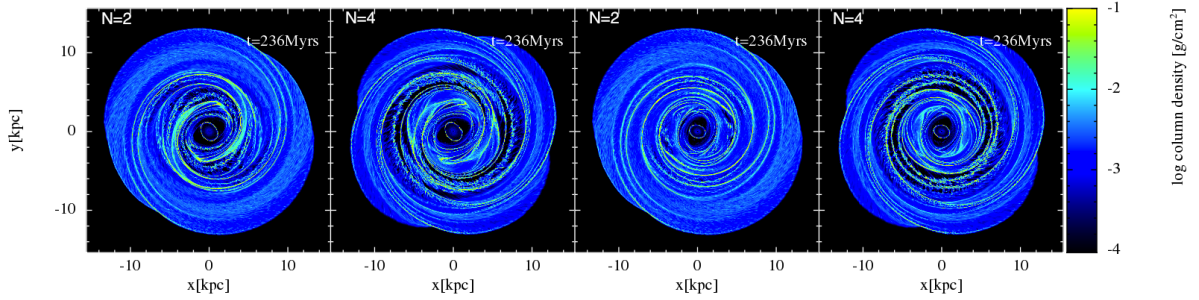


Figure 4.12: Top-down maps of the gaseous response to the different $N - \Omega_b$ potential pairs, all of which have $\alpha = 12^\circ$, $\Omega_{sp} = 20 \text{ km s}^{-1} \text{ kpc}^{-1}$ and evolved for 236 Myrs. The bar potential in the left panels has $\Omega_b = 50 \text{ km s}^{-1} \text{ kpc}^{-1}$, and $\Omega_b = 60 \text{ km s}^{-1} \text{ kpc}^{-1}$ in the right panels, shown in conjunction with 2 and 4 armed models.

The slower bars disrupt the arm features up to the Solar radius, while the faster bars are less radially extended, allowing arms to approach smaller radii. The 2-armed models still have a dearth of high density interarm material, though the arms in conjunction with the slower bar has additional interarm structure caused by the large radial extent of the features driven by the bar (though this is more evident at later times).

4.6.2 Simple kinematic maps

An additional complication to the barred-spiral models is the offset between the arm and bar potentials, which is time-dependent due to $\Omega_{sp} \neq \Omega_b$. By choosing to analyse the model at specific time-stamp, as in the arm and bar only simulations, we would have already selected the offset between the bar and arm features. Instead we analysed each barred-spiral model in the range of 280-370 Myrs, regardless of arm number and bar pattern speed. This range was the minimum required time between arm passages around a reference frame aligned with the bar for all models considered and includes the full possible range of arm-bar offsets.

To actually determine the best-fitting arm-bar offset we use the same fitting method to fit the observer's coordinates for the arm and bar calculations, leaving R_{obs} and V_{obs} free. We fixed the bar at $\theta_b = 45^\circ$, effectively fixing l_{obs} , which is consistent with the best fitting value found in our bar-only simulations. This allows for a reference point for altering the arm-bar offset. This method has one major caveat, we must assume the morphological features do not change considerably in the time-frame used to perform the fit, approximately 100 Myrs. Global arm and bar features tend to stay the same over this time frame, with the main difference seen in the gas around the OLR of the bar, effectively where the bar meets the arms. At this radius the material from the bar driven arms has altering substructure and begins to wrap around into a ring-like structure.

This process is illustrated by Figures 4.13 and 4.14, showing the fit statistic and corresponding $l-v$ maps for a calculation with $N = 2$, $\Omega_b = 50 \text{ km s}^{-1} \text{ kpc}^{-1}$ and $\alpha = 15^\circ$. Figure 4.13 shows the behaviour of the fit statistic with varying observer position and velocity, and with varying time (which dictates the arm-bar offset). A clear broad minimum can be seen around 320 Myrs, with corresponding values of $R_{\text{obs}} = 8.5 \text{ kpc}$ and $V_{\text{obs}} = 220 \text{ km s}^{-1} \text{ kpc}^{-1}$. Figure 4.14 shows the $l-v$

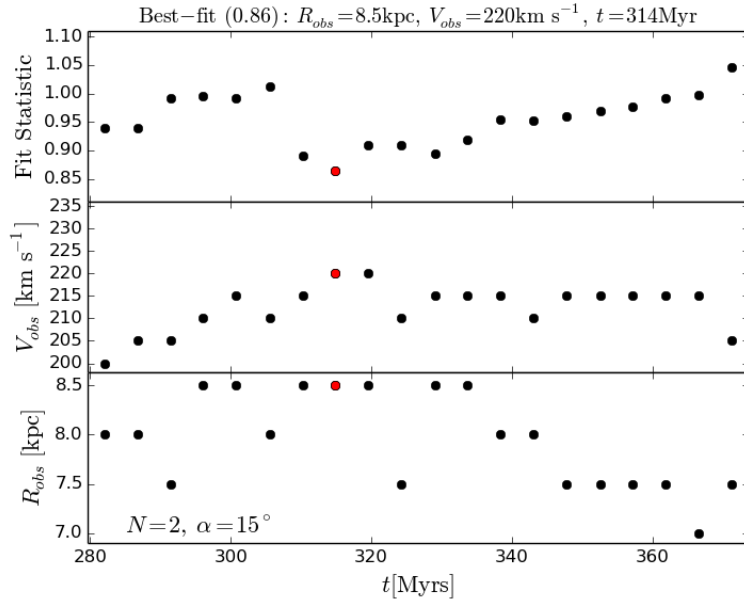


Figure 4.13: Variation of fit statistic with evolution of a barred spiral galaxy (top panel) which is used to constrain the arm-bar offset. The model here has $N = 2$, $\Omega_b = 50 \text{ km s}^{-1} \text{ kpc}^{-1}$ and $\alpha = 15^\circ$. The best fitting time-frame is indicated by the red point. Corresponding l - v maps are shown in Figure 4.14. Middle and lower panels show the best-fitting values of R_{obs} and V_{obs} at the same epochs.

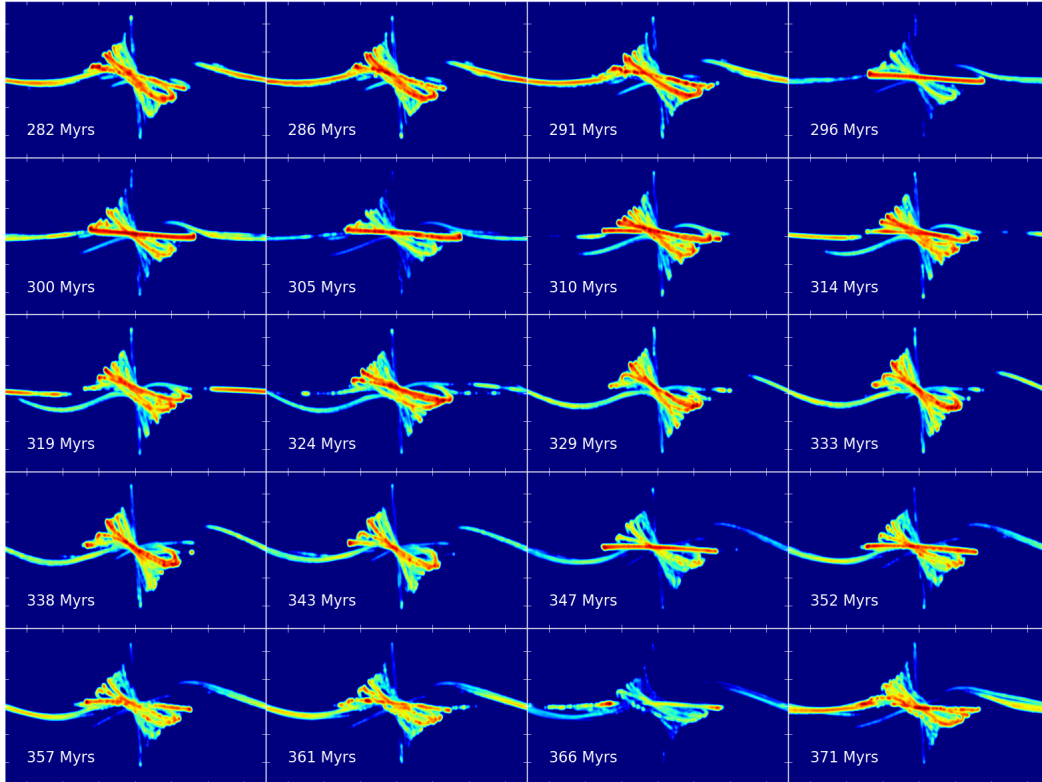


Figure 4.14: Evolution of kinematic l - v maps for a barred spiral galaxy with changing arm-bar offset. Each panel corresponds with a point shown in Figure 4.13.

maps for each point in Figure 4.13, constructed using the best-fit parameters. This figure shows the motion of arm features with respect to the bar, where individual arms can be seen to move vertically in velocity space with time. Conversely inner features caused by the bar (where $|v_{\text{los}}| \gg 0$) can be seen to not change. The final panel in Fig. 4.14 has the same arm-bar offset as a time between the third and fourth panels (around 294Myrs). While differences between the maps can be seen, the global structure is the same, showing that over the time-frame of 100Myrs the l - v features vary only marginally.

4.6.3 Radiative transfer maps

The TORUS emission maps for each N - Ω_b - α combination are shown in Figure 4.15 with the best fitting values of R_{obs} , V_{obs} and arm-bar offset (i.e. evolution time) found using the method described in Section 3.6. The best-fitting values for each model are also given in Table 4.1. Simple by-eye comparisons between these maps shows that whilst most fit some features well ultimately none shown a perfect match to the data, suffering the same problems as the arm-only models in Chapter 3. As was the case in the arm only models, the fit statistic is uncorrelated with the pitch angle. If the fit statistic is averaged across all parameters except pitch angle then there is a marginal preference towards $\alpha = 12.5^\circ$. There is also a preference towards a pattern speed of $\Omega_b = 50\text{km s}^{-1} \text{kpc}^{-1}$ for $N = 2$ models and $\Omega_b = 60\text{km s}^{-1} \text{kpc}^{-1}$ when $N = 4$.

The reasons preventing a good fit to all emission features are covered by the following examples. In Fig. 4.16 we show four different arm-bar simulations from Fig. 4.15 in both l - v and x - y space. These have been chosen to highlight the main differences between the simulations, and are not necessarily the best fits from Fig. 4.15. In the first panel we show a 2-armed spiral model with our slower bar ($50\text{km s}^{-1} \text{kpc}^{-1}$). The l - v map in this case shows a good reproduction of the Carina arm, and Local arm material in the second quadrant (this is common to all 2-armed model fits in Fig. 4.15). The x - y map shows that the l - v Carina arm feature in this model actually joins with the Local arm material. The Carina segment branches away as it nears the Solar position, passing through $R < R_\odot$ while the Local arm feature breaks away from the spiral potential and maintains a radial distance of $R > R_\odot$ upon passage into the first quadrant. The major drawback of this and other 2-armed models is the failure to produce the Outer, Perseus and Local arms simultaneously. Two armed-models produce an inner emission ridge seen in observations (a combination of the Scutum-Centaurus-Crux, SCC, arms and possibly a molecular ring). However the ridge in this case is too shallow in l - v space, implying it is too close to the Solar position.

In the second panel we show another 2-armed model with a moderate pitch angle (12.5°) and a slow bar ($50\text{km s}^{-1} \text{kpc}^{-1}$), but with a slower arm pattern speed than the previous model ($15\text{km s}^{-1} \text{kpc}^{-1}$). This value of Ω_{sp} provides strong branching features that can be seen in the x - y map, driving a 4-armed gas structure from only a 2-armed potential. This model reproduces the Perseus, Outer and the Local arms. Reproducing these arm features simultaneously would be impossible for a 2-armed logarithmic structure (as in the previous model). The Local and Outer arms are actually reproduced by the branches, not the arms directly tracing the potential. The SCC arm/inner ridge is angled similarly to observations, and the 3kpc-expanding arm is very clearly seen in l - v space. The main flaw in this model is the position of the Carina arm, which does not

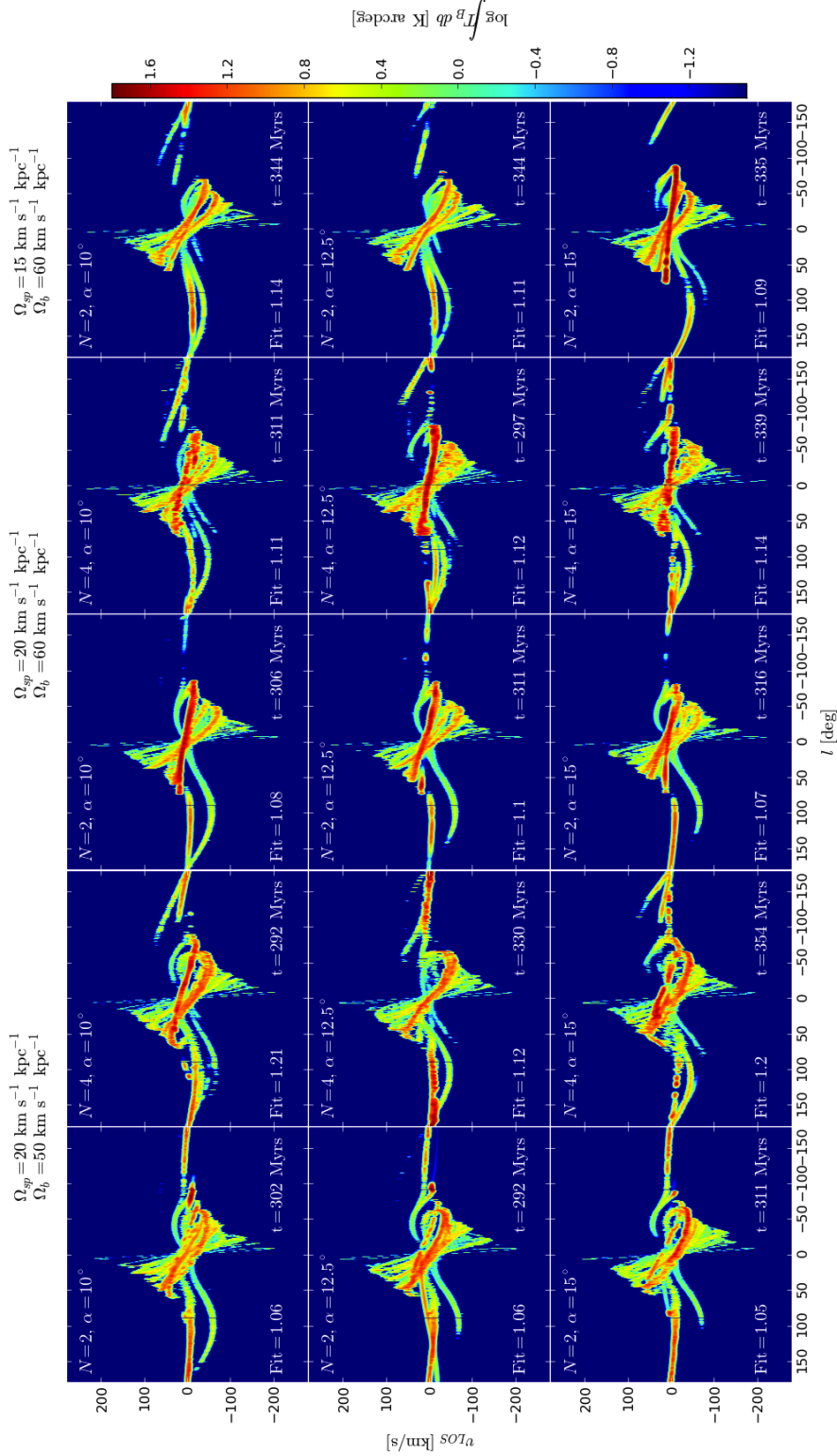


Figure 4.15: Synthetic emission maps made using `torus` for our barred-spiral models with $\theta_b = 45^\circ$. The arm position relative to the bar is found using the method of fitting to the observer coordinates in the isolated arm and bar cases. The first two columns show $\Omega_b = 50 \text{ km s}^{-1} \text{ kpc}^{-1}$ with $N = 2, 4$ respectively, and the second two show $\Omega_b = 60 \text{ km s}^{-1} \text{ kpc}^{-1}$ with $N = 2, 4$. The fifth column has a slower arm pattern speed of $\Omega_{sp} = 15 \text{ km s}^{-1} \text{ kpc}^{-1}$. The spiral arm pitch angle increases from top to bottom.

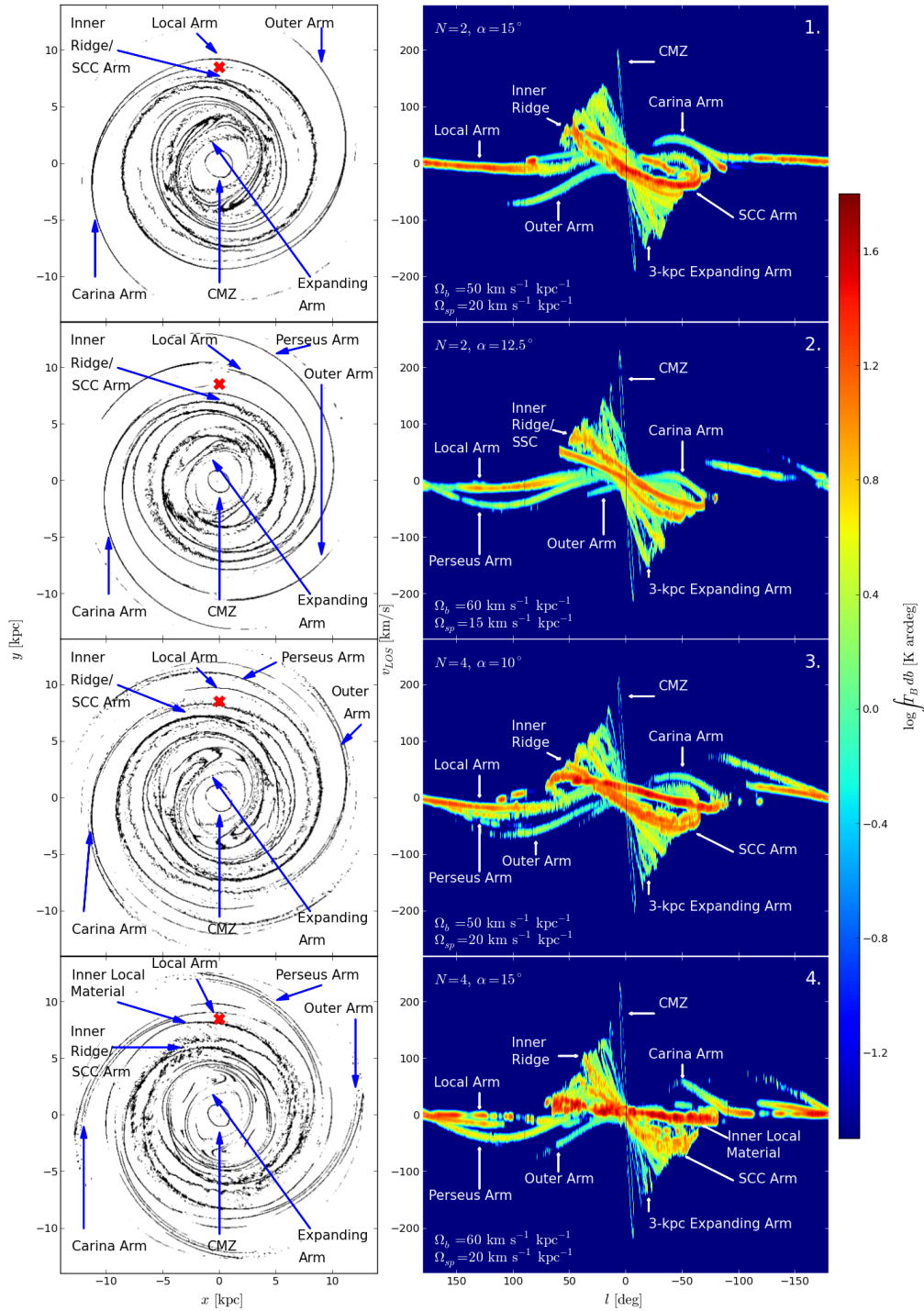


Figure 4.16: Four CO radiative transfer l - v maps with their x - y counterparts from Fig. 4.15, chosen to show a range of different morphologies. The top-down maps only show material that is seen in CO l - v space; that of the highest density. The cross indicates the observer's position (which differs between models). SCC refers to the Scutum-Centaurus-Crux arm in the 4-armed paradigm of the Milky Way, also referred to in the main text as the Inner Ridge. Arrows indicate locations of prominent features in l - v space. Models 2 and 4 reproduce the outer arm structure while 1 and 3 provide a better reproduction of the Carina arm.

reach into the $v_{los} > 0 \text{ km s}^{-1}$ region as seen in observations.

The third panel shows a 4-armed model with a shallow pitch angle (10°). In this case there is clear reproduction of the Carina arm feature, located inside the Solar radius in x - y space. As this feature passes in between the Solar position and the Galactic centre it causes a bright emission feature at near-local velocities, a feature not seen in observations. The SCC arm feature is seen behind this strong emission feature in l - v space. The second quadrant arm features are not as clear as the previous model, with the Local and Perseus features not clearly separated in l - v space. The feature here labelled as the Outer arm could equally be labelled the Perseus arm, but would leave multiple arm structures unidentified in the outer Galaxy, caused by a large amount of branching material in the $7\text{kpc} < R < 11\text{kpc}$ region seen in x - y space.

Best fit parameter	Mix model	
	CGN2+WK	CGN4+WK
Ω_b [$\text{km s}^{-1} \text{kpc}^{-1}$]	50	60
V_{obs} [km s^{-1}]	220	215
R_{obs} [kpc]	8.5	8.5
α [$^\circ$]	15	10

Table 4.1: Best fitting values for the barred-spiral simulations. A systematic uncertainty for each value is present due to the coarseness of the parameter space; $\Delta\Omega_{sp} = \Delta\Omega_b = 10\text{km s}^{-1} \text{kpc}^{-1}$, $\Delta V_{\text{obs}} = 5 \text{ km s}^{-1}$, $\Delta R_{\text{obs}} = 0.5\text{kpc}$ and $\Delta\theta_b = 10^\circ$. The parameter space for the mix models is smaller than the isolated cases and was refined in Chapter 3.

The final panel also shows a 4-armed model, with a wide pitch angle (15°), but with a faster bar than the previous panels ($60\text{km s}^{-1} \text{kpc}^{-1}$). The faster bar is less extended radially, allowing the gas to trace the spiral potential to smaller radii. In the x - y map the spiral arm pitch angle is maintained to $R \approx 4\text{kpc}$, whereas in the slower, $50\text{km s}^{-1} \text{kpc}^{-1}$, models in the upper panels structure is dominated by the bar until $R \approx 6\text{kpc}$. This model appears to produce all the observed features; Local arm, Perseus arm, Outer arm, SCC arms/ridge and Carina arm. The problem again is that arms must pass in front of the observer to appear in the fourth quadrant, producing emission that dominates the SCC feature in the inner Galaxy. This model in particular has little emission in the third quadrant, as seen in observations, owing to the Perseus arm disappearing as it leaves the second quadrant. The Carina arm feature is located at higher values of v_{los} than is seen in observations, however there are similar maps for the $\alpha = 12.5^\circ$ case that provide a better match for this section, but are not shown in this figure due to the poor reproduction of other features.

Do the arms and bar have the same pattern speed?

Results presented in this and the previous chapter indicated that the bar and arms have different pattern speeds, a view that is supported by numerous other studies of our Galaxy (see the review of Gerhard 2011). This is also seen in some numerical simulations of disc galaxies, where patterns in the inner disc tend to rotate considerably faster than those in the outer disc (Sellwood & Sparke 1988; Grand et al. 2012). Observations of external galaxies however often favour a single, or smoothly decreasing pattern speed with radius (Egusa et al. 2009; Speights & Westpfahl 2011, 2012), as do some other numerical studies (Roca-Fàbrega et al. 2013). To check the validity of

a model with independent bar and spiral pattern speeds we performed calculations where both components have the same pattern speed, primarily to check whether the smaller parameter space of the previous section (where $\Omega_{sp} = 20 \text{ km s}^{-1} \text{ kpc}^{-1}$) was justified.

In Figure 4.17 we show calculations with barred, 2-armed, and 4-armed potentials, and their combinations where $\Omega_{sp} = \Omega_b$ in the range of $10\text{-}60 \text{ km s}^{-1} \text{ kpc}^{-1}$, using the WK and CG potentials. The effect of adding a bar can clearly be seen in the third and fifth rows, with the main difference being the addition of the inner x_2 orbits. In the case of the faster bars ($50, 60 \text{ km s}^{-1} \text{ kpc}^{-1}$) the bar tends to dominate the spiral features which are confined within $R < 8 \text{ kpc}$ where the OLR of the bar drives strong ring-like structures. The slower pattern speeds ($10, 20 \text{ km s}^{-1} \text{ kpc}^{-1}$) the bar has a minimal effect on the arm structures, only dominating the morphology within $R < 3 \text{ kpc}$. This is due to the OLR of the bar lying well outside the Galactic disc at these slow pattern speeds. The mid-range speeds ($30, 40 \text{ km s}^{-1} \text{ kpc}^{-1}$) show morphologies effected by the bar and spiral features now that the bar and spiral OLR is within the disc. This is clearer in the 4-armed case, where the arm OLR lies at a smaller radii than that of the bar.

The slowest pattern speed calculations do not appear to produce desirable morphological structures. In the 2-armed case the bar is barely noticeable, leaving effectively just the arms and we have already shown that the $\Omega_{sp} = 10 \text{ km s}^{-1} \text{ kpc}^{-1}$ arm models provide a poorer fit than the $20 \text{ km s}^{-1} \text{ kpc}^{-1}$ case. The 4-armed case has weak arm and bar features, which are not strong enough to maintain a sufficient CO abundance to appear in $l\text{-}v$ emission maps. The faster models are far too radially constrained to reproduce the observed $l\text{-}v$ features, with arms only persisting well within the Solar radius, making it impossible to reproduce the Perseus and Outer arms.

The remaining pattern speeds ($20\text{-}50 \text{ km s}^{-1} \text{ kpc}^{-1}$) display both arm and bar features. Figure 4.18 shows $l\text{-}v$ maps of the models in Figure 4.17 with pattern speed of $20\text{-}50 \text{ km s}^{-1} \text{ kpc}^{-1}$. These maps were made using the simple method described in Chapter 3 and are shown for the best fitting R_{obs} , V_{obs} and l_{obs} (where the bar is constrained to point towards the second quadrant). As the arm and bar features rotate with the same pattern speed, we have assumed some fixed arm-bar offset. As such the exact position of features is not expected to perfectly reproduce those seen in observations, but rather show $l\text{-}v$ morphologies possible with single pattern speeds. The $20 \text{ km s}^{-1} \text{ kpc}^{-1}$ models allow for a large amount of spiral structure, but the bar forms some peculiar inner structures due to the large inner x_2 orbits which creates wide loop-like structures in $l\text{-}v$ space. The faster, $50 \text{ km s}^{-1} \text{ kpc}^{-1}$, bar has ILR inside the Solar radius, so the bar-driven arms lie in the inner Galaxy, creating emission with less gaps, and central emission that better resembles observations. The $40 \text{ km s}^{-1} \text{ kpc}^{-1}$ model suffers the same problems as the bar-only models of Chapter 3, where the OLR of the bar lies just inside the Solar radius. This causes very strong emission at local velocities in the inner Galaxy, which is absent in observations. Finally, the $50 \text{ km s}^{-1} \text{ kpc}^{-1}$ model has very few arm features in the outer Galaxy, as the arms are now within, or just outside for $N = 2$, the Solar radius, making it impossible to fully represent the arm features in the outer Galaxy.

None of the barred spiral models shown above with $\Omega_{sp} = \Omega_b$ seem to be able to reproduce Galactic $l\text{-}v$ features better than models with $\Omega_{sp} \neq \Omega_b$. Bar features do a good job of fitting the central emission for fast pattern speeds, while arm models better represent the outer Galaxy with

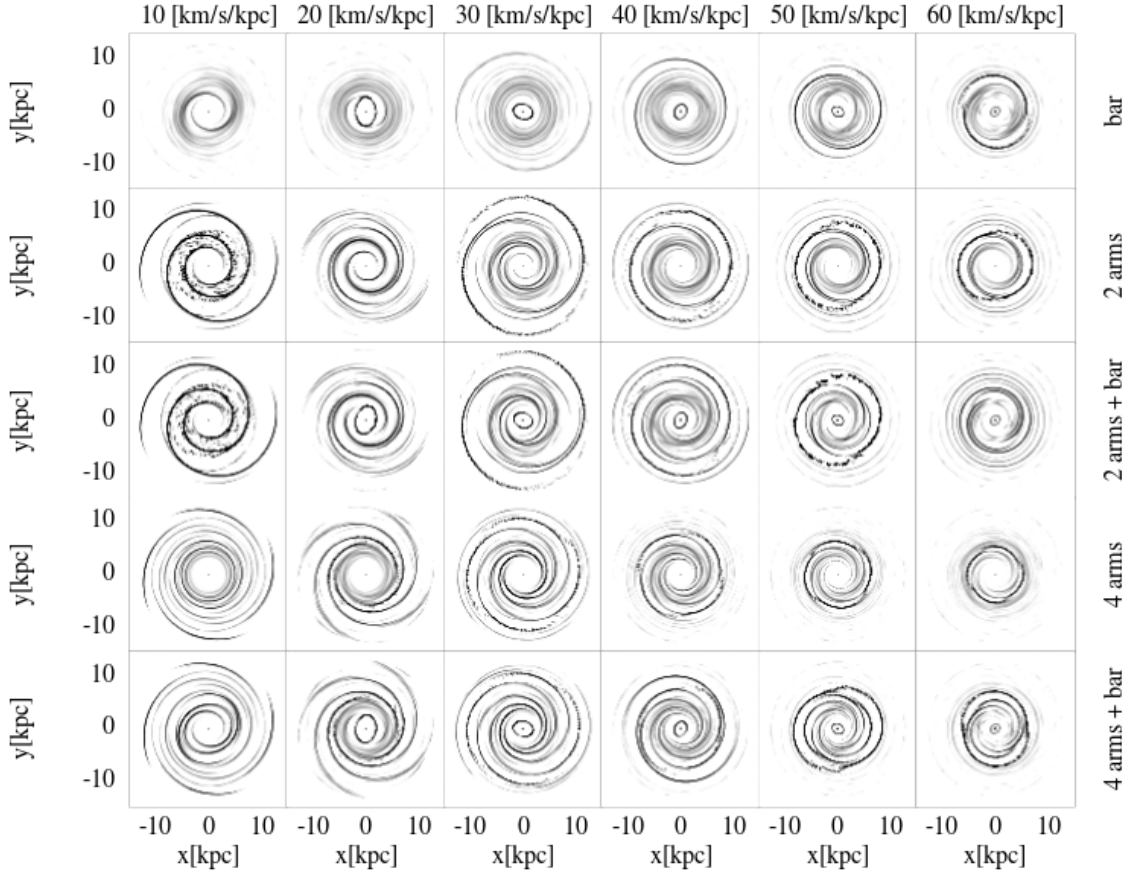


Figure 4.17: Top down views of calculation with bar and arm potentials rotating at the same pattern speed, increasing from left to right. The different rows show, in order from top to bottom, bars, 2-armed models, 2-armed and a bar, 4-armed, 4-armed and a bar, all after 380Myrs of evolution. A black and white scheme is used to highlight the minor differences in the addition of a bar to the central region.

slow pattern speeds. This leads us to the conclusion that the CO features of the Milky way are best represented with two very different pattern speeds for the arms and bar.

The central molecular zone

In all of our l - v maps we fail to reproduce the structure of the CMZ. In certain instances we do produce velocities that are comparable to the highest values seen in observations, one such example is shown in Fig. 4.19. The peak velocity structures in our models stem from the inner x_2 bar orbits perpendicular to the bar major axis, and appear as a symmetric loop structure in l - v space, while the observed CMZ is highly asymmetric. The SPH particles that are present have aligned themselves with the x_2 orbits, leaving little material available to fill in the missing emission. In order to fully capture the asymmetric emission features in the central galaxy a dedicated simulation is required of only the inner galaxy to better resolve the gaseous features. The addition of stellar feedback or a live stellar disc may also be required to break up the symmetric inner bar orbits.

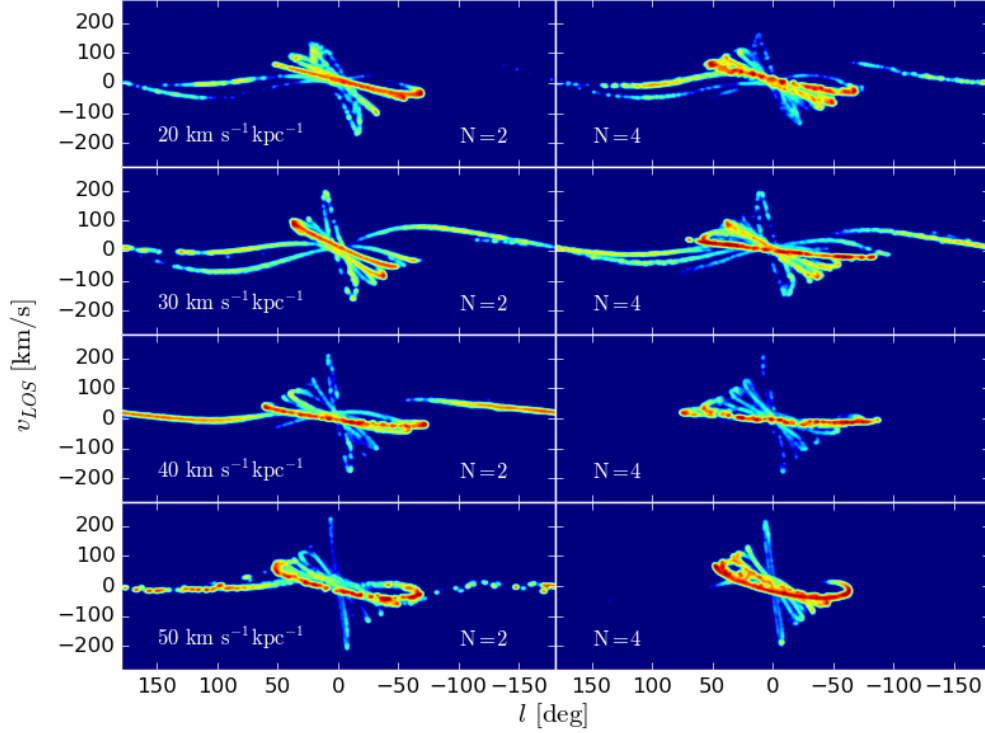


Figure 4.18: Best fitting l - v maps of the calculations shown in Fig. 4.17 with arm/bar pattern speeds of 20, 30, 40 and $50 \text{ km s}^{-1} \text{ kpc}^{-1}$ (increasing from top) and $N = 2$ or $N = 4$. These are simple kinematic maps, rather than being built by torus, where the bar is allowed to lie anywhere within the second quadrant.

It may be the case that the bar model is correct, but the physics is too simple to correctly model the l - v features. The x_2 orbital features are aligned similarly to the CMZ. Lee et al. (1999) constrained the x_2 orbits of a barred model to the CMZ features, finding that while a wide orientation angle of $\theta_b = 50^\circ$ provided a good reproduction of the l - v slope, the gas particles traced very thin structures in l - v space similar to those in Fig. 3.18. They did however perform a similar calculation with collisionless N -body particles, representing the stellar component, which appear much broader in l - v space similar to observations. In the next chapter we will be discussing calculations with a live stellar component, which also may provide a better match to observations.

4.7 Discussion of investigation using spiral and bar potentials

The models shown in Figures 4.15 and 4.16 show it is possible to reproduce all features of the l - v data. However, we find it difficult to produce a good match to all features simultaneously. Four armed models are more capable of fitting multiple features simultaneously, but to do so must place some arm structure just inside the Solar position. This must be within very close proximity to allow the tangent point of the Carina arm to reach out to $l \approx -90^\circ$. While a strong emission feature is seen in the inner Galaxy in observations, it is angled much steeper in l - v space than our synthetic maps. One can conclude that the local SCC arm material is either lacking in molecular

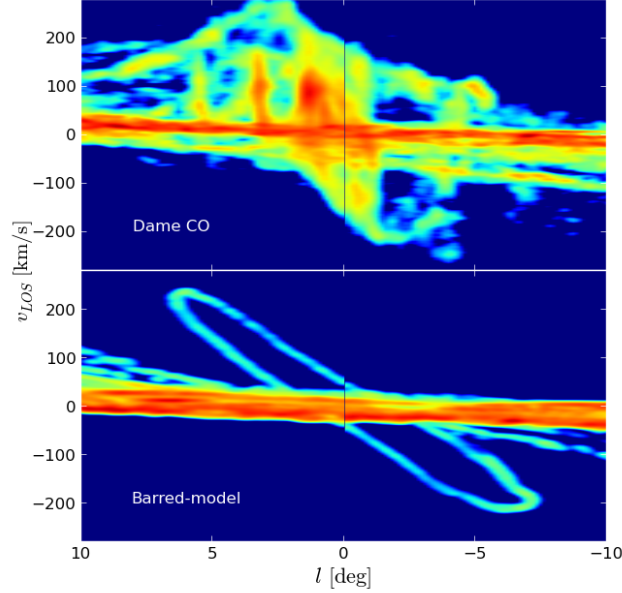


Figure 4.19: The observed CO emission in the Galactic centre (top, $|l| < 10^\circ$) compared to that produced in the centre by the addition of a barred potential rotating at $50 \text{ km s}^{-1} \text{ kpc}^{-1}$ (bottom). The underlying model appears too simplistic to capture the large amount of structure seen in observations.

material or that the shape is far from that of a logarithmic spiral near the Solar position. If it is indeed lacking in molecular gas, then it can be expected to at least be rich in atomic gas.

Alternatively the Carina-Sagittarius arm structure could deviate significantly from a normal logarithmic-spiral structure. This is supported by other works in the literature (e.g. Georgelin & Georgelin 1976, Pandian et al. 2008). These models involve some straight section of the SCC arm as it passes in front of the observer. In Fig. 4.20 we show such a model, specifically that of Taylor & Cordes (1993), compared to a 4-fold symmetric spiral pattern similar to that used in this study. This additional distance between the observer would give the arm a greater line-of-sight velocity, pulling it up and away from the $V_{los} = 0 \text{ km s}^{-1}$ line in our maps in Fig. 4.15, as seen in projection in the bottom left panel of Fig. 4.20. It is also seen in observations that while the Sagittarius and Carina tangents are well traced by distance determinations, there is very little material placed on these arms in the local Galaxy in the direction of the Galactic centre (e.g. Georgelin & Georgelin 1976, Fish et al. 2003, Russeil 2003, Hou et al. 2009). It also may be that the arm structure is better represented by a transient and irregular spiral structure, rather than that of a fixed grand design galaxy. These structures are reproducible in simulations through the inclusion of a live stellar disc, rather than fixed analytical potential (e.g. Baba et al. 2009; Dobbs et al. 2010; Grand et al. 2012).

In Gómez & Cox (2004) the authors construct synthetic l - v maps by simply mapping structures in x - y onto l - v co-ordinates. They too show that while the Carina “hook” is easy to reproduce, it causes a strong dense ridge angled far too shallow in l - v space compared to that seen in observa-

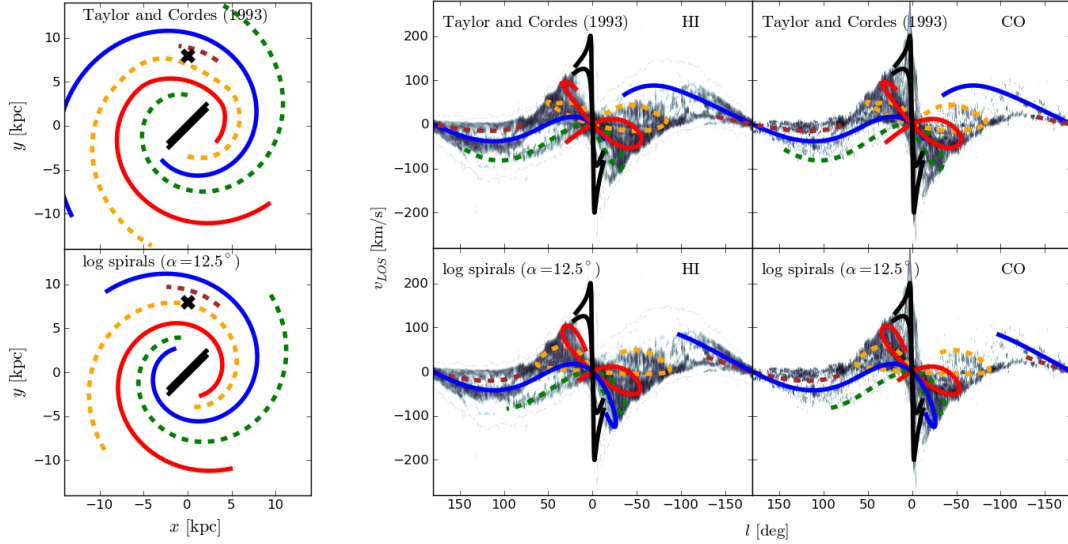


Figure 4.20: Different arm models in x - y plane (top figure) and their projection onto l - v space (bottom figure). Left panels: arm model of modified logarithmic spirals from Taylor & Cordes (1993), primarily constrained to data from Georgelin & Georgelin (1976). Right panels: simple 4-armed spiral model with each arm offset by $\pi/2$ from the previous with addition of a local arm segment. Arms only extend radially to distance required to match l - v emission features. Observed CO and HI emission data is plotted on greyscale behind the model arm features in the lower figure. Bold lines indicate the strong primary arm features in the old stellar population inferred by Churchwell et al. (2009).

tions. They also note that crowding in velocity space can cause ridges in l - v space not necessarily corresponding to high density gas regions. As CO traces high density regions only we do not have that problem here, and our l - v features correspond well with high density gas regions associated with arm and bar features. Our results are at some odds with the work by Rodriguez-Fernandez & Combes (2008), who find that a bar pattern speed of $30\text{km s}^{-1} \text{kpc}^{-1}$ is the best match to the l - v diagram, without the inclusion of arm potentials. Our value is more in keeping with that suggested by Fux (1999), $50\text{km s}^{-1} \text{kpc}^{-1}$, and Englmaier & Gerhard (1999), $50\text{-}60\text{km s}^{-1} \text{kpc}^{-1}$. Our lower pattern speed of $40\text{km s}^{-1} \text{kpc}^{-1}$ resulted in extremely strong emission in front of the observer, features that would not appear in the aforementioned works due to the mapping of x - y features to l - v space lacking a radiative transfer treatment.

4.8 Chapter summary

In this Chapter we have built on the work in presented in Chapter 3. We have constructed the first synthetic emission maps in CO and HI of the full Galactic plane using the radiative transfer code `TORUS`. Spiral and bar features can clearly be seen in l - v space, with emission of comparable strengths to that seen in observations. While CO features seemed only to scale in strength with surface density, the HI emission experiences very strong absorption at the higher surface densities

needed to observe considerable CO emission. We believe this to be a result of the simplistic nature of the physics in the calculation, with gas readily falling into a very thin plane, increasing optical depth and HI absorption. However, CO is well reproduced, which is a better tracer of spiral structure.

We then performed calculations similar to those in Chapter 3 but with the inclusion of arm and bar potentials simultaneously. While these provide a better reproduction of observations than the arm or bar models could alone, even with these we could not satisfactorily reproduce all the observed CO features. Whilst it was possible to reproduce features in emission that are seen in observations, such as the Perseus arm, Carina arm, inner ridge emission, local material and the outer arm, these features are not all reproducible simultaneously. The 2-armed models cannot reproduce all these features, yet the 4-armed models create too much emission locally. Assuming logarithmic spiral arms, in order to successfully match the Carina arm feature, an extremely strong emission feature must be placed near $v_{los} = 0 \text{ km s}^{-1}$ in the inner Galaxy. Models which do not use radiative transfer may miss the significance of this feature. Alternatively the Carina arm would need to exhibit an irregular shape in the vicinity of the Sun. This leads us to the conclusion that while the 4-armed symmetrical model can produce many of the features seen in the l - v observations, it may be necessary to allow an irregular arm structure to convincingly match the Galaxy.

The possibility of the arm and bar components rotating at the same pattern speed was also investigated. These models did a significantly poorer job however than those with $\Omega_{sp} \neq \Omega_b$, implying the bar and arms are both morphologically and kinematically different entities.

An alternative approach to that in this and the previous Chapter is to model the Milky Way as a transient, multi-armed galaxy by the inclusion of a live N -body stellar disc. A study of the Milky Way ISM l - v emission using a live-stellar disc, and the comparison to the grand design case, is the topic of the subsequent Chapter.